9ᵗʰ International Workshop on Microsystems

Alexander Campus, International Hellenic University, 11 December 2024

Workshop Proceedings

Introduction

This workshop brings together research and development from a large spectrum of science and engineering fields related to the implementation of microsystems in the new era of distributed information technologies. As cloud computing services and smart portable systems are becoming ubiquitous and more advanced, new possibilities for interdisciplinary research emerge. The microsystems that comprise the so-called internet of things will encompass a wide range of technologies including new energy sources, energy and information electronics, sensor systems, smart and energy efficient control and computing, telecommunications and networking, and also nanotechnology and micro-electro-mechanical systems. Continuing eight successful workshops between 2016 and 2023, the 9th International Workshop on Microsystems aims at bringing together related research and development advancements from the academic community and the industry. Scientific topics include but are not limited to:

Microelectronics and nanoelectronics	Industrial automation and control
Embedded systems	Micro-electro-mechanical systems
Sensors and sensor electronics	Computing for microsystems
Integrated circuits and systems	Energy microsystems

Michail E. Kiziroglou

m.kiziroglou@ihu.gr

Venue

Lecture Theater, Automation and Informatics Building

Alexander Campus, International Hellenic University, Greece
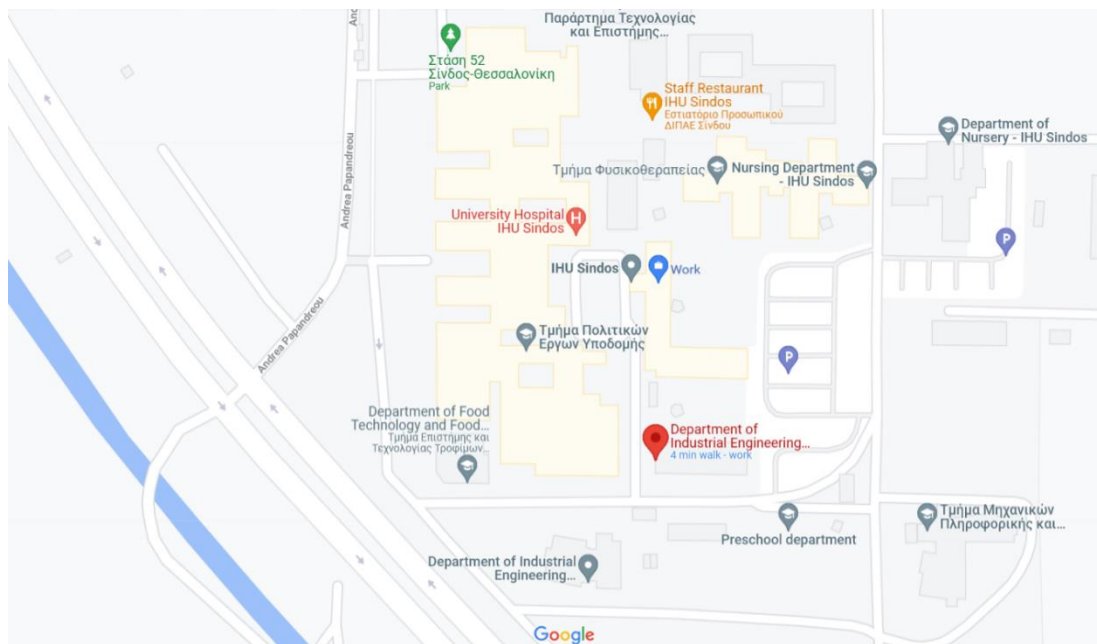
Date

Wednesday, 11th of December, 2024

Organizer

Michail E. Kiziroglou

Session Chairs

Dr. Vasilis Pavlidis, Aristotle University of Thessaloniki, Greece

Dr. Eirini Aivazidou, Industrial Engineering & Management, IHU, Greece

Dr. Theodoros Kosmanis, Industrial Engineering & Management, IHU, Greece

Dr. Dimitrios Tziourtzioumis, Industrial Engineering & Management, IHU, Greece

Technical Programme Committee

Alexandros Astaras	Fotis Stergiopoulos
Dimitrios Bechtsis	Nikolaos Tampouratzis
Alkiviadis Hatzopoulos	Dimitrios Tziourtzioumis
Michail E. Kiziroglou	Apostolos Tsagaris
Theodoros Kosmanis	Dimitris Triantafyllidis
Simira Papadopoulou	Christos Yfoulis
Kostas Siozios	

Organization and Technical Support

Panagiotis Kappas, Ippokratis Kochliaridis

List of Authors

No	Last Name	First Name	Affiliation
1	Andronikos	K.	Spacedot Ltd, Greece
2	Antoniadou	A.	IEM, International Hellenic University, Greece
3	Athanasiadis	Angelos	Aristotle University of Thessaloniki, Greece
4	Drakaki	Maria	Department of Science and Technology, IHU, Greece
5	Hatzopoulos	Argyrios T.	IEE, International Hellenic University, Greece
6	Inglezos	Charalampos	IEM, International Hellenic University, Greece
7	Kiziroglou	Michail E.	IEM, International Hellenic University, Greece
8	Kochliaridis	Ippokratis	IEM, International Hellenic University, Greece
9	Kosmanis	Theodoros I.	IEM, International Hellenic University, Greece
10	Koumides	Chrysostomos	Aristotle University of Thessaloniki, Greece
11	Kyriazopoulou	A.	IEM, International Hellenic University, Greece
12	Liamos	D	IEE, International Hellenic University, Greece
13	Meimaroglou	E.	IEM, International Hellenic University, Greece
14	Michailidou	Maria	Aristotle University of Thessaloniki, Greece
15	Michalas	Loukas	Democritus University of Thrace, Greece
16	Moustakas	V. P.	Spacedot Ltd, Greece
17	Mpalsis	Th.	Spacedot Ltd, Greece
18	Nikolaides	John	IEM, International Hellenic University, Greece
19	Ntabizas	Anastasios	Department of Science and Technology, IHU, Greece
20	Papadopoulou	Maria S.	IEE, International Hellenic University, Greece
21	Papaefstathiou	Ioannis	Aristotle University of Thessaloniki, Greece
22	Pavlidis	Vasilis F.	Aristotle University of Thessaloniki, Greece
23	Rouka	Evanthia	Aristotle University of Thessaloniki, Greece
24	Soulaki	K. M.	IEM, International Hellenic University, Greece
25	Tampouratzis	Nikolaos	IEM, International Hellenic University, Greece
26	Tapoglou	Nikolaos	IEM, International Hellenic University, Greece
27	Tatsoglou	I.	Spacedot Ltd, Greece
28	Terzis	Vasileios	IEM, International Hellenic University, Greece
29	Tsiakmakis	Kyriakos	IEE, International Hellenic University, Greece
30	Tzionas	Panagiotis	IEM, International Hellenic University, Greece
31	Tziourtzioumis	Dimitrios N.	IEM, International Hellenic University, Greece
32	Vamvakas	P.	Spacedot Ltd, Greece
33	Vassios	V. D.	IEE, International Hellenic University, Greece
34	Xenofontos	George	IEE, International Hellenic University, Greece

Programme

08:45-09:00: Registration

Please check-in or register at the front desk.

09:00-09:15: Welcome and introduction

09:15-10:00: Keynote Speech

Energy-Efficient Communication in 2.5D Integrated Systems, *Vasilis F. Pavlidis*, Aristotle University of Thessaloniki, Greece, 24WOM-01 (Invited)

10:00-11:00: First Oral Session (Session Chair: Vasilis F. Pavlidis, AUTH)

10:00-10:30: PeakSat OBC design & Environmental Testing Results. *I. Tatsoglou, P. Vamvakas, K. Andronikos, Th. Mpalsis and V. P. Moustakas*, *Spacedot Ltd*, 24WOM-02 (Invited)

10:30-10:45: Energy-Efficient FPGA Framework for Non-Quantized Convolutional Neural Networks, *A. Athanasiadis, N. Tampouratzis, I. Papaefstathiou*, 24WOM-03

10:45-11:00: Smart-Irrigation Monitoring System using IoT Technology, *G. Xenofontos, Ch. Koumides, K. Tsiakmakis, A. T. Hatzopoulos and M. S. Papadopoulou*, 24WOM-04

11:00-11:30: Coffee Break and Poster Session

P1. Analyzing Trends and Focus Areas in Neuromodulation Research, *M. Michailidou, Ch. Inglezos and E. Rouka*, 24WOM-05 (withdrawn)

P2. Study of Vegetation Health Indicators: GNDVI and Leaf Area Index in Precision Agriculture Applications, *D. Liamos, K. Tsiakmakis, A. T. Hatzopoulos, V. Vassios and M. Papadopoulou*, 24WOM-06

P3. The geometry of smart building blocks and its programming, *J. Nikolaides and D. Bechtsis*, 24WOM-07

11:30-12:45: Second Oral Session (Session Chair: Eirini Aivazidou, IHU)

11:30-12:00: Micro-Electro-Mechanical Systems for high frequency implementations, *L. Michalas,* 24WOM-08 (Invited)

12:00-12:15: Development of a Data Acquisition and Data Logging Platform, *V. Terzis and N. Tapoglou*, 24WOM-09

12:15:-12:30: Acoustic Power Transfer Through Solid Surfaces, *I. Kochliaridis and M. E. Kiziroglou*,   24WOM-10

12:30-12:45: Emerging Technologies for Effective Humanitarian Crisis Management, *A. Ntabizas, M. Drakaki and P. Tzionas*, 24WOM-11

12:45-13:00: Best Paper Award by Ioannidis Electronics.

13:15 Third Oral Session (Session Chairs: Th. Kosmanis and D. Tziourtzioumis, IHU)

13:15-13:30: Development of a data acquisition system for underwater environmental measurements, *A. Antoniadou, Th. Kosmanis and D. Tziourtzioumis*, 24WOM-12

13:30-13:45 Design and construction of a data recording system for the powertrain of an electric vehicle, *A. Kyriazopoulou, Th. Kosmanis and D. Tziourtzioumis*, 24WOM-13

13:45-14:00 Design and construction of a data acquisition device for a gasoline internal combustion engine management system, *E. Meimaroglou, D. Tziourtzioumis and Th. Kosmanis*, 24WOM-14

14:00-14:15 Implementation of a single beam echosounder sonar for the generation of bythometric maps, *K. M. Soulaki, D. Tziourtzioumis and Th. Kosmanis,* 24WOM-15

WORKSHOP PAPERS

Energy-Efficient Communication in 2.5D Integrated Systems (INVITED)

Vasilis F. Pavlidis

Department of Electrical and Computer Engineering

Aristotle University of Thessaloniki

e-mail: vpavlid@ece.auth.gr

Abstract:

Chiplet integration with advanced 2.5D integration technologies, such as interposers, enables increased bandwidth among chiplets through either wide and slow buses (e.g., AIB) or high speed Ser/Des circuits (e.g., PCIe). This talk presents a data encoding technique for each of these communication approaches that decreases the energy demand for data transfers among chiplets [1], [2]. The advantage of the methods compared to prior art originates from modeling the Hamming distance among successive pieces of data as delays in the time domain. The encoding circuit implementing this approach is depicted in Fig. 1. Both simulation and experimental results are presented for a diversity of application workloads that are typical in high-performance computing. The energy gains of the method including the overhead of the en/decoding circuits are described. Lastly, related tradeoffs among energy, bandwidth, latency, and bit error rate are discussed, demonstrating the efficiency and usefulness of the method.
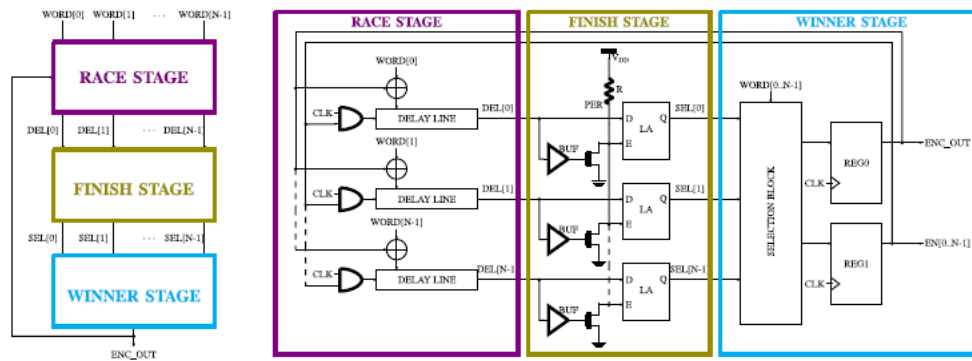
Fig. 1. Encoder circuit.

[1]. E. Maragkoudaki, W. Toms, and V. F. Pavlidis, "Energy-Efficient Encoding for High-Speed Serial Interfaces," *IEEE Transactions on Very Large Scale Integration (VLSI) Systems*, Vol. 30, No. 10, pp. 1484-1496, October 2022.

[2]. E. Maragkoudaki and V. F. Pavlidis, "Energy-Efficient Time-Based Adaptive Encoding for Off-Chip Communication," *IEEE Transactions on Very Large Scale Integration (VLSI) Systems*, Vol. 28, No. 12, pp. 2551-2562, December 2020.

Bio: Vasilis F. Pavlidis is an Associate Professor in the ECE Department of Aristotle University of Thessaloniki, Greece. He holds an MSc and PhD degree from the University of Rochester, Rochester, NY, obtained in 2003 and 2008, respectively, all in Electrical and Computer Engineering. From 2008 to 2012, he was a post-doc at the Integrated Systems Laboratory of EPFL, Switzerland. He has 10+ years of research experience in the areas of on-chip interconnect modelling and design and emerging technologies, such as 3-D integration and spintronics. He is the leading author of the book Three-Dimensional Integrated Circuit Design, (1st and 2nd Editions) and contributor to the software tool, Manchester Thermal Analyzer. He has delivered over 20 invited talks in academia, research centers, and industry, including a 5-day course on 3-D integration at the University of Beihang, China. He is a Senior member of the IEEE and offers editorial service for several IC design and VLSI journals, such as IEEE TVLSI and IEEE TCAD.

PeakSat OBC design & Environmental Testing Results

I. Tatsoglou, P. Vamvakas, K. Andronikos, Th. Mpalsis and V. P. Moustakas

Abstract: PeakSat is the second satellite developed by the Spacedot team. PeakSat is a 3U CubeSat mission designed in the Aristotle University of Thessaloniki. It aims to demonstrate the capability of performing laser links with Optical Ground Stations in Greece and to pave the way for a space-based quantum communications network. This paper focuses on the On-Board Computer of the satellite and describes the board's design as well as the results of the environmental tests the board has undergone before it was deemed adequate to handle the tasks it is designed for. The On-Board Computer (OBC), often referred as the brain of the satellite, is responsible for managing control laws, data processing, health monitoring, and data handling. The PeakSat OBC is a modified version of AcubeSat's design, adapted to the mission needs. Key components include a Microcontroller, the Power supply unit and peripherals such as the memories, temperature sensors and the CAN and RS422 transceivers. To ensure mission reliability, the underside of the PCB features a redundant OBC with almost all the functionality of the upper side, ready to take place in the event of failure. For the OBC to be considered suited for launch, the board has undergone various environmental tests that revealed design flaws and software errors that shaped the final design. These tests, conducted at the Tartu Observatory in Estonia and the CubeSat Support Facility in Belgium, simulated the harsh conditions expected during launch and in orbit, including vibration (VIBE) and thermal vacuum (TVAC) tests.

SpaceDot Bio: SpaceDot is an interdisciplinary, non-profit, research team, based in the Aristotle University of Thessaloniki, but extending to multiple institutions across Greece and Europe. The main goal of SpaceDot is to develop the space engineering sector in Greece and to promote it and make it accessible to anyone through its core open-science philosophy. The primary two projects SpaceDot is developing at the moment is AcubeSAT, a biological nanosatellite aiming to study the effects of microgravity and radiation to eukaryotic cells, and PeakSat, a nanosatellite aiming to establish high-speed and secure, free-space optical communication with the optical ground station developed by AUTh in Holomondas. AcubeSAT is supported by the "Fly Your Satellite!" 3 program by the European Space Agency (ESA) education office, and PeakSat is part of the "Greek CubeSats In-Orbit Validation" supported by ESA and the Greek Ministry of Digital Governance.
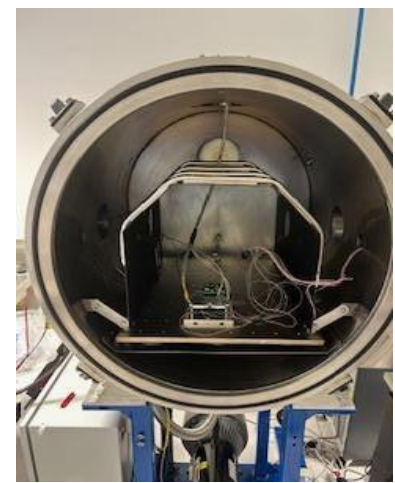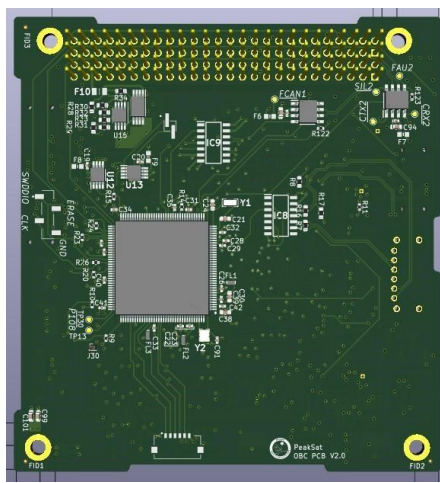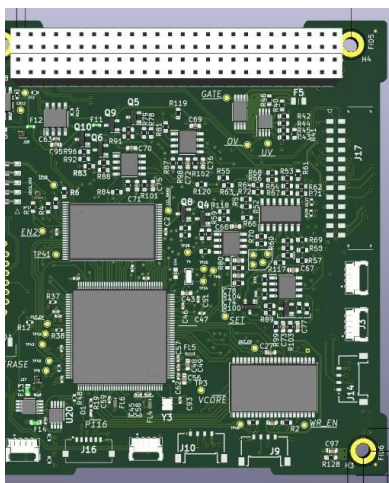
Energy-Efficient FPGA Framework for Non-Quantized Convolutional Neural Networks

Angelos Athanasiadis[1], Nikolaos Tampouratzis[2], Ioannis Papaefstathiou[1]

Department of Electrical & Computer Engineering, Aristotle University of Thessaloniki, Greece[1]
Department of Industrial Engineering & Management, International Hellenic University, Greece[2]
Email: angelathan@ece.auth.gr; ntampouratzis@ihu.gr; ygp@ece.auth.gr

Abstract—**The growing demand for real-time processing in artificial intelligence applications, particularly those involving Convolutional Neural Networks (CNNs), has highlighted the need for efficient computational solutions. Conventional processors, very often, fall short in balancing performance, power consumption, and latency, especially in embedded systems and edge computing platforms. Field-Programmable Gate Arrays (FPGAs) offer a promising alternative, combining high performance with energy efficiency and reconfigurability. The presented framework addresses the complex and demanding computations of CNNs on FPGAs maintaining full precision in all neural network parameters. Specifically, our framework is based on Darknet which is very widely used for the design of CNNs and allows the designer, by using a similar input to that given to Darknet, to efficiently implement a CNN in a heterogeneous system comprising of CPUs and FPGAs. When compared with the FPGA frameworks that support quantization, our solution aims to offer similar performance and/or energy efficiency without any degradation on the NN accuracy.**

Keywords—High-Performance Computing; Neural Networks; Matrix Multiplication; AMD FPGA; Vitis

I. INTRODUCTION

In the recent years, Convolutional Neural Networks (CNNs) are the key components for many significant advancements in the field of artificial intelligence. They have proven to be highly effective in numerous fields like image, video and natural language processing. Additionally, they are effective in various tasks including image classification, object detection, and semantic segmentation. It often encounters difficulties like high processing power and power consumption. The complicated structures of CNNs, which consist of several convolutional layers, fully connected layers, and a large number of parameters, require significant computational resources which can be a substantial barrier, particularly for applications that demand real-time processing and need to be deployed on devices with limited resources, such as embedded systems and edge computing platforms.

Various approaches [1],[2],[3] have been proposed to implement CNNs focusing mainly in heavily quantized models. Non-quantized models maintain the full precision of the network parameters, ensuring high accuracy at the cost of higher resource utilization and power consumption. Quantized models, on the other hand, reduce the precision of the parameters, thereby lowering resource usage and power consumption but very often at the cost of reduced accuracy.

In this paper we present a novel design and implementation framework that allows for the seamless FPGA implementations of non-quantized CNNs with high performance, energy efficiency and accuracy. The main benefits of our approach are:

- **Accuracy Preservation:** By avoiding quantization and retaining full precision, the proposed framework aims to preserve the accuracy of the CNN models.

- **High Design Productivity, Flexibility and Adaptability:** The presented efficient design flow is based on the widely used DarkNet CNN design framework, it is based on purely C/C++ and targets the whole range of FPGAs from the smallest to the largest ones.

- **High Performance:** The proposed framework can fully exploit the parallelism of any FPGA to accelerate the inference process of CNNs, ensuring timely and efficient processing.

- **Energy Efficiency:** The proposed framework optimizes the power efficiency of CNN inference on FPGAs, making it suitable for power-sensitive applications.

II. FRAMEWORK ARCHITECTURE

Figure 1 presents the framework architecture of our framework which handles convolutional and deconvolutional layers within neural networks in an automated manner. This architecture is represented as a flowchart, emphasizing the sequential and parallel processes involved in the tool's operation.
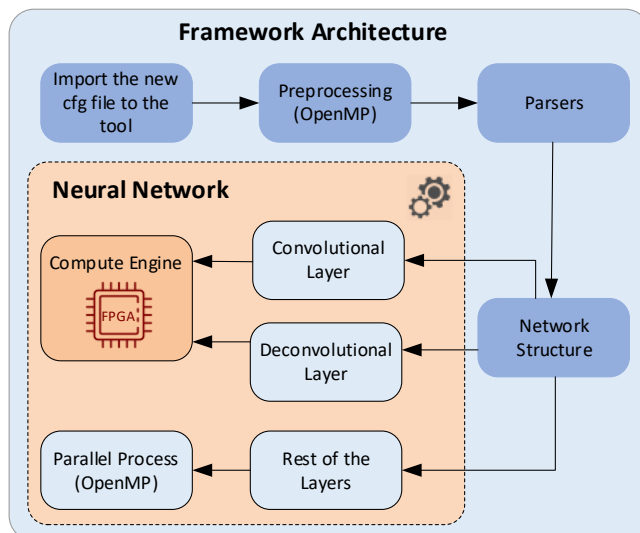

Figure 1: Architecture of the Framework

The key element is the Innovative Compute Engine using High Level Synthesis (HLS) on FPGA, which allows the execution of multiple mathematical executions in a single clock cycle achieving a relatively high throughput and performance.

III. Implementation of Innovative HLS Compute Engine

Our HLS FPGA Kernel handles mainly the matrix multiplication tasks which is the cornerstone in virtually every CNN implementation. Moreover, as illustrated in Figure 2, we utilize the internal BRAMs in conjunction with HLS streams, to optimize also the on-chip memory access patterns and further increase the computational efficiency.
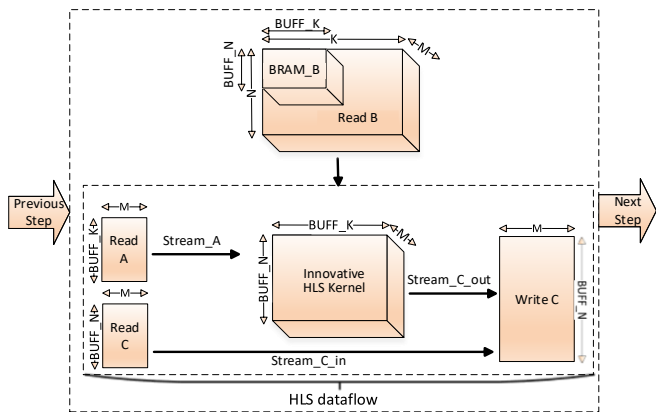

Figure 2: Architecture of Innovative Compute Engine

The aforementioned outcome leads to a significant decrease in the effective latency associated with off-chip memory retrieval and guarantees the accessibility of data for computational purposes, thereby diminishing idle time caused by external memory latency. Specifically, streams enable a continuous flow of data between processing elements without the need for intermediary storage in BRAMs, minimizing the latency and resource overhead. By leveraging streams, data is transferred directly between producer and consumer processes, facilitating pipelined execution and enhancing parallelism. This direct transfer mechanism reduces the dependency on BRAMs for temporary storage, leading to more efficient resource utilization and higher throughput. Furthermore, streams can handle variable data rates more effectively ensuring that processes are not overwhelmed by the rate of data production.

In addition, modern FPGAs are connected to multiple memory banks with dedicated channels (e.g., multiple DRAM modules or HBM lanes) in order to increase the external memory bandwidth. In order to take advantage of those multiple lanes/modules we insert the appropriate HLS directives that split data transfers into a parameterizable number of memory banks/lanes so as to take full advantage of the bandwidth available in each of the memory interfaces. The transfers of data between the central processing unit (CPU) and the field-programmable gate array (FPGA) are facilitated at the full data width (512 bits) per clock cycle, thereby ensuring high-throughput communication between the processing elements and memory subsystems.

IV. Experimental Results

To demonstrate further the effectiveness of the presented approach we compare the non-optimized reference model, the fully optimized model on both a high-end FPGA (AMD Alveo U55C) and an embedded one (Kria KR260), the parallel execution of matrix multiplication using OpenMP in a multicore CPU and using CUDA on an NVIDIA T4 GPU. In all experiments the array dimensions which are M=2048, K=4096, and N=16384 are selected so as to be different from those triggering our peak performance demonstrating the

flexibility of our approach (since it can effectively handle any shape of matrices).
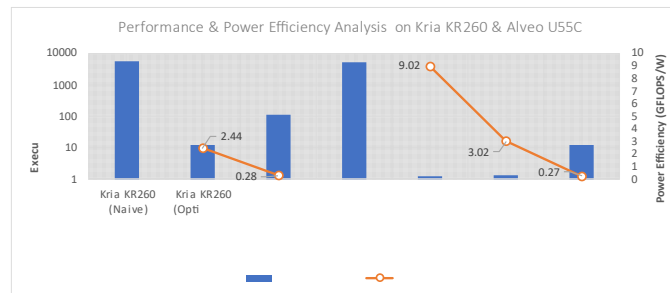

Figure 3: Performance and Power Efficiency Analysis (FP32)

Furthermore, the results obtained from numerous experiments with different dimensions are fully inline with those presented in Figure 3. As illustrated in this figure, our fully-optimized implementation for the embedded FPGA is two orders of magnitude faster than the reference implementation and 9x times faster compared to the fully parallelized algorithm executed on an embedded ARM 4core CPU (Cortex-A53); those numbers include all the memory accesses and the external memory technologies and topologies are exactly the same. Similarly, our fully optimized approach when implemented on the Alveo U55C board is approximately three orders of magnitude faster than the reference implementation and 10x times faster compared to the fully parallelized algorithm executed on an Intel Xeon E5-2620 v4 (8 cores). In order to further compare the overall efficiency of the presented approach with that triggered by the software implementation, the GFLOPS/Watt for each implementation were also measured. Based on our measurements we achieve 34x and 9x higher energy efficiency than the best CPU parallel implementation in an Alveo U55C and a Kria KR260 respectively. Moreover our design, when implemented on the Alveo, is 3x more power efficient than the CUDA implementation on an NVIDIA T4 GPU which is also implemented on a better CMOS technology (12nm for T4 vs 16nm for U55c).

V. Conclusion

In conclusion, this research addresses the critical need for efficient CNN implementations in power-constrained environments. The proposed non-quantized FPGA-enabled CNN framework successfully combines high performance with energy efficiency, leveraging the inherent parallelism and reconfigurability of FPGAs. By maintaining full precision in network parameters, the framework achieves high accuracy without compromising on resource utilization or power consumption. The experimental results validate the framework's effectiveness, showing substantial speedups in inference processing and significant reductions in power usage.

References

[1] Xu, Y.; Luo, J.; Sun, W. Flare: An FPGA-Based Full Precision Low Power CNN Accelerator with Reconfigurable Structure. Sensors 680 2024, 24

[2] Chen, J.; Liu, L.; Liu, Y.; Zeng, X. A Learning Framework for n-Bit Quantized Neural Networks Toward FPGAs. IEEE Transactions on Neural Networks and Learning Systems 2021, 32, 1067–1081.

[3] Latotzke, C.; Ciesielski, T.; Gemmeke, T. Design of High-Throughput Mixed-Precision CNN Accelerators on FPGA. In 666 Proceedings of the 2022 32nd International Conference on Field-Programmable Logic and Applications (FPL), 2022, pp. 358–365.

Smart-Irrigation Monitoring System using IoT Technology

George Xenofontos[1], Chrysostomos Koumides[2], Kyriakos Tsiakmakis[1], Argyrios T. Hatzopoulos[1], Maria S. Papadopoulou[1]*

[1] Department of Information and Electronic Engineering
International Hellenic University
57400 Sindos, Thessaloniki, GREECE
[2] School of Electrical and Computer Engineering,
Faculty of Engineering, Aristotle University of Thessaloniki
54124, Thessaloniki, GREECE
email: * mspapa@ihu.gr

Abstract—**This paper presents a smart and sustainable plant development monitoring system that utilises IoT technology to enhance automated irrigation and environmental monitoring. The system uses an ESP32-C3 microcontroller integrated into a custom PCB to monitor soil moisture, temperature, and humidity in real-time, optimising irrigation and conserving water. The design is suitable for precision agriculture and smart gardening, providing remote monitoring capabilities via a web application with Firebase and Google Sheets. With direct and solar power supply options, the project aims to promote both convenience and sustainability.**

KeyWords—**Smart-Irrigation, IoT, ESP32, Real-Time monitoring, Solar power, Electronic circuits**

I. INTRODUCTION

Precision agriculture and smart gardening are rapidly gaining importance due to their potential for enhancing efficiency and sustainability [1]. Recent studies have highlighted the importance of precision agriculture and smart-irrigation in improving crop yields, reducing resource wastage, and enhancing overall sustainability [2]-[4]. This is particularly crucial in the face of climate change and increasing global food demand [5]. This paper discusses an IoT-based system developed to monitor plant health and automate irrigation using a custom hardware setup. The proposed system is built on an ESP32-C3 microcontroller, custom PCB, and several sensors to provide an efficient way to manage irrigation and monitor plant conditions [6]-[7]. The primary goals of the system include real-time data collection, remote monitoring, and efficient irrigation management to improve plant health while conserving water [8]-[10]. In this paper, we present the detailed design, system components, workflow, and testing results, demonstrating the potential of this technology to support sustainable agriculture.

II. SYSTEM ARCHITECTURE

The design and implementation of the environmental monitoring system for plant care were underpinned by a comprehensive selection of materials and a methodical approach to ensure the success of the project. This section outlines the specific materials used, the technologies employed, and the detailed process followed to implement the final system.

A. Hardware Components

The system architecture consists of both hardware and software components, each contributing to the overall efficiency and reliability of the plant monitoring and irrigation system. The core of the hardware is the ESP32-C3 microcontroller, which manages sensor data collection and cloud communication. The ESP32-C3 is particularly well-suited for IoT-based agricultural applications due to its integrated Wi-Fi and Bluetooth capabilities.

A custom PCB is used to integrate all system components, providing a modular, plug-and-play platform. This custom PCB shown in Fig. 1 houses connectors for sensors and power management, enhancing reliability and simplifying installation.

The system relies on several sensors for monitoring: the DHT11 sensor is used for measuring ambient temperature and humidity, the DS18B20 sensor provides temperature data for the root zone, and the Gravity Analog Soil Moisture Sensor V2 (SEN0114) of DFRobot measures soil moisture, triggering irrigation when required. The soil moisture sensor consists of two nickel-plated probes that measure the volumetric water content by utilizing soil's electrical resistance. It provides analog outputs from 0 to 3V, where 0V indicates water saturation and 3V for dry soil. The sensor operates at 3.3-5.0V and has a built-in voltage regulator for stable readings. When soil moisture drops below 68%, indicating insufficient

water content for mint growth, the ESP32-C3 processes this analog signal to trigger the irrigation system through the relay. Also, supports both direct power supply and solar power as energy sources. The direct power supply ensures stable operation indoors, while the solar panel provides an option for off-grid and outdoor applications, thus promoting sustainability. The system is powered by a 6W solar panel (267x177mm) which provides sustainable energy for outdoor deployments. The solar power unit, connected via voltage regulator to prevent overcharging, ensures continuous operation of the ESP32-C3 and sensors while maintaining stable voltage levels required for accurate sensor readings. The irrigation system is actuated by a 12V DC pump, which is controlled by a 5V relay, activated by the ESP32-C3 based on soil moisture levels.
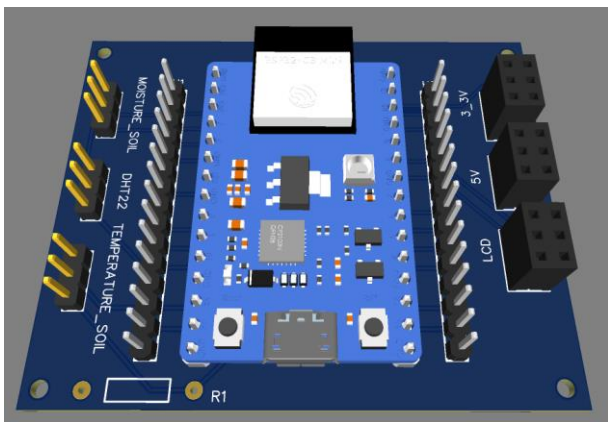
Fig. 1. PCB with uC and sensors

Fig. 2 shows the implemented proposed system, while Fig. 3 illustrates hardware architecture. The ESP32-C3, sensors, power sources, and irrigation components are integrated into the system.
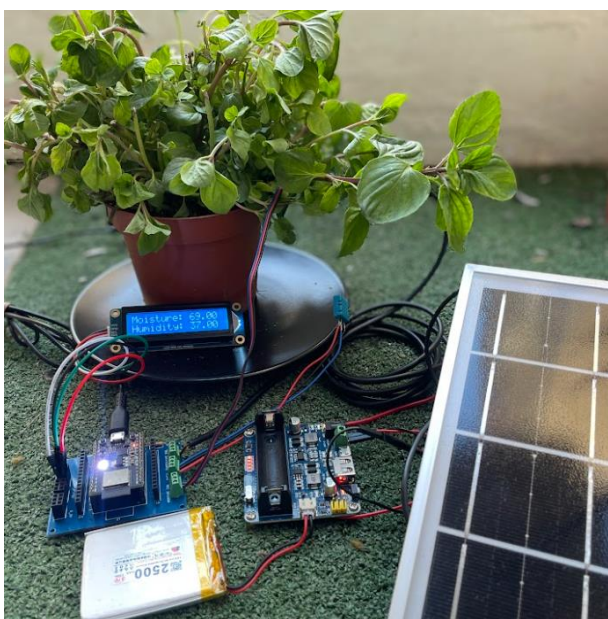
Fig. 2. The implemented proposed system
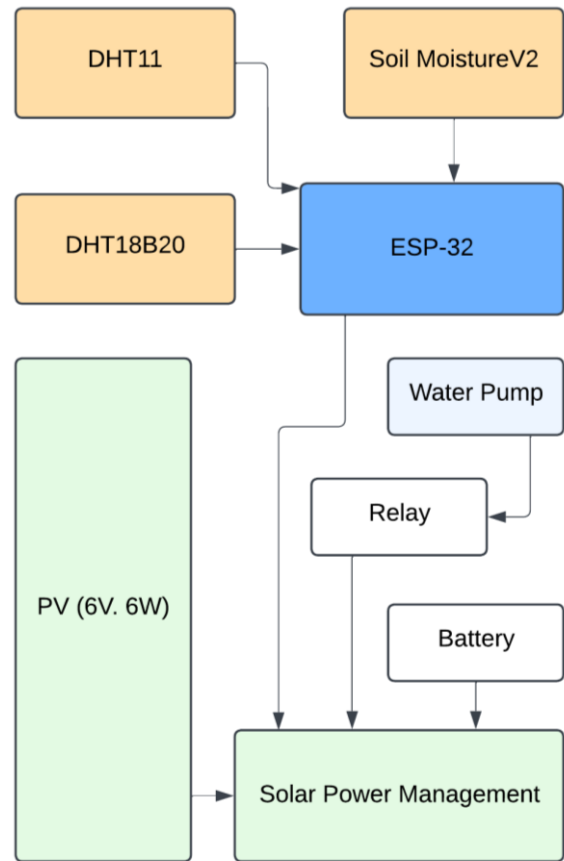
Fig. 3. Diagram of hardware connections and configurations

B.   Software Components

The software includes Firebase Realtime Database, Google Sheets integration, and a web application. The Firebase Realtime Database provides cloud storage for sensor data, enabling real-time remote monitoring of plant conditions. The integration with Google Sheets allows for easy synchronisation of the data using Google Script, making it accessible and analysable for users without requiring advanced database skills. The web application developed using HTML, CSS, Bootstrap, EJS, jQuery and JavaScript, allows users to monitor real-time data and manually control irrigation, if needed. Backend operations are managed using Node.js and Express.js.

The web application design, as shown in Fig. 4, provides users with an intuitive dashboard for monitoring plant conditions and managing the irrigation system.
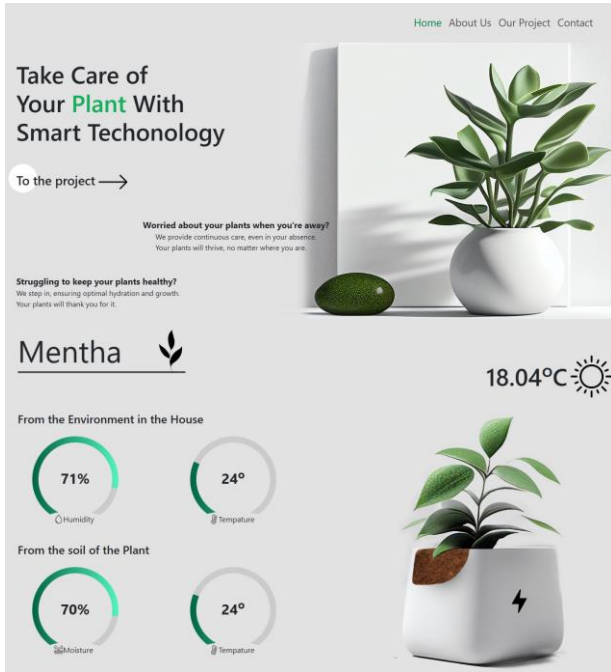
Fig. 4. Figma design of the Dashboard and Contact Us page demonstrating a minimal and simple style

Fig. 5. Workflow of the proposed system

III. SYSTEM WORKFLOW

The system workflow begins with data collection, where the ESP32-C3 gathers data from the DHT11, DS18B20, and Moisture sensors, measuring temperature, humidity, and soil moisture. Based on the soil moisture data, the ESP32-C3 makes decisions regarding irrigation. When soil moisture falls below a predefined threshold (68%), the ESP32-C3 activates the water pump to ensure that the plants receive optimal water supply. The flowchart of the workflow is shown in Fig. 5. The collected sensor data is transmitted to Firebase in real-time, allowing users to access it remotely. Additionally, the data is logged in Google Sheets for statistical analysis, providing a convenient way to track changes over time. Users can access real-time data and control the irrigation system through the web application, which also allows for manual intervention when necessary.

IV. RESULTS

Testing our IoT-based irrigation system on mint plants showed significant improvements in both plant health and water efficiency [11]. Mint requires consistent moisture between 70% and 75% for optimal growth. By automating irrigation based on real-time soil moisture data, the system reduced water usage by approximately 30% compared to manual watering, aligning with findings on the resource-saving benefits of precision agriculture technologies [2]-[3]. The DS18B20 temperature sensor accurately monitored soil and ambient temperatures with $\pm0.5°C$ precision, while the DHT11 sensor tracked humidity levels, essential for maintaining mint's ideal growing conditions. Data was stored in Firebase and Google Sheets, allowing for continuous monitoring and easy analysis. Fig. 6 illustrates soil moisture over a 12-day period, showing that the automated system maintained optimal conditions for mint growth more effectively than manual methods.

In comparison to other IoT-enabled plant monitoring systems, such as that of Hossain et al. [6], our system demonstrated superior water efficiency for mint. Future improvements may focus on further enhancing sensor accuracy and expanding adaptability for various plant types [12].

V. CONCLUSIONS

The presented IoT-enabled plant monitoring and irrigation system offers a scalable and sustainable solution for smart agriculture. It combines real-time monitoring, automated decision-making, and remote accessibility to improve both plant health and water efficiency.

Fig. 6. Measurement of soil moisture level in 12 trial days with smart-(auto) and manual- irrigation

Future work will focus on enhancing the system's autonomy and predictive capabilities, making it a robust tool for precision agricultu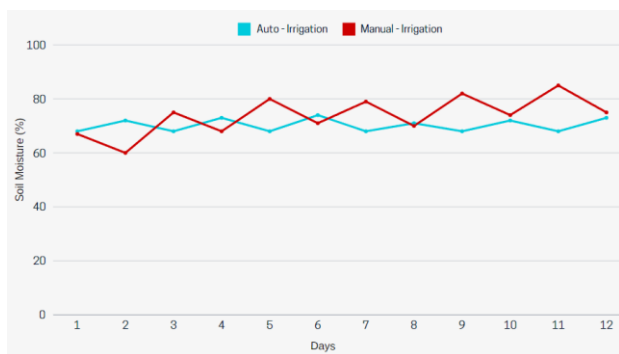re and smart gardening. By leveraging the ESP32-C3, a custom PCB, and cloud-based data management, this system demonstrates how IoT technology can contribute to more efficient and sustainable plant care, providing significant value for both individual gardeners and large-scale agricultural operations.

REFERENCES

[1] Sustainable Agriculture Initiative, "The Role of Precision Agriculture in Sustainable Farming Practices," *Sustainable Agriculture*, 2023. [Online]. Available: https://www.sustainableagriculture.eco/post/the-role-of-precision-agriculture-in-sustainable-farming-practices. [Accessed: Nov. 2, 2024].

[2] S. Mohanty and S. Misra, "Advancements in Precision Agriculture for Enhancing Crop Yields and Sustainability," in *Innovative Technologies for Precision Agriculture*, Springer, 2022, pp. 235–245. doi: 10.1007/978-3-031-26692-8_14.

[3] A. D. Boursianis et al., "Smart Irrigation System for Precision Agriculture—The AREThOU5A IoT Platform," in IEEE Sensors Journal, vol. 21, no. 16, pp. 17539-17547, 15 Aug.15, 2021, doi: 10.1109/JSEN.2020.3033526.

[4] L. Preite, F. Solari, and G. Vignali, "Technologies to Optimize the Water Consumption in Agriculture: A Systematic Review," Sustainability, vol. 15, no. 7, 2023, doi: 10.3390/su15075975.

[5] Financial Times, "How Climate Change is Reshaping Global Food Demand," *Financial Times*, 2023. [Online]. Available: https://www.ft.com/content/99958fff-8f69-42ca-b90b-5e2e2677845b. [Accessed: Nov. 2, 2024].

[6] M. Hossain, M. Islam, and D. Kim, "IoT-Enabled Plant Health Monitoring System for Smart Agriculture," *Sensors*, vol. 23, no. 4, Art. no. 1002, 2023. doi: 10.3390/s23123423.

[7] A. D. Boursianis et al., "Advancing Rational Exploitation of Water Irrigation Using 5G-IoT Capabilities: The AREThOU5A Project," 2019 29th International Symposium on Power and Timing Modelling, Optimization and Simulation (PATMOS), Rhodes, Greece, 2019, pp. 127-132, doi: 10.1109/PATMOS.2019.8862146.

[8] Circuit Digest, "Smart Irrigation System Using ESP32 and Blynk App," *Circuit Digest*, 2023. [Online]. Available: https://circuitdigest.com/microcontroller-projects/smart-irrigation-system-using-esp32-and-blynk-app. [Accessed: Nov. 2, 2024].

[9] A.D. Boursianis et al., "Internet of Things (IoT) and Agricultural Unmanned Aerial Vehicles (UAVs) in smart farming: A comprehensive review," Internet of Things, vol. 18, p. 100187, 2022, doi: https://doi.org/10.1016/j.iot.2020.100187.

[10] G. Xenofontos and M.S. Papadopoulou, "Automated Plant Irrigation System Using Arduino Microcontroller," presented at the 4th International Conference in Electronic Engineering, Information Technology & Education, May 2023, pp. 96–100.

[11] A. Hafian, M. Benbrahim, and M. N. Kabbaj, "Design and Implementation of Smart Irrigation System Based on the IoT Architecture," in *Digital Technologies and Applications*, S. Motahhir and B. Bossoufi, Eds., Cham: Springer, 2021, vol. 211, pp. 345–354, doi: 10.1007/978-3-030-73882-2_32.

[12] L. García, L. Parra, J. M. Jimenez, J. Lloret, and P. Lorenz, "IoT-Based Smart Irrigation Systems: An Overview on the Recent Trends on Sensors and IoT Systems for Irrigation in Precision Agriculture," *Sensors*, vol. 20, no. 4, p. 1042, Feb. 2020, doi: 10.3390/s20041042.

Study of Vegetation Health Indicators: GNDVI and Leaf Area Index in Precision Agriculture Applications

Liamos D., Tsiakmakis K., Hatzopoulos, A.T., Vassios V., and Papadopoulou M.

Department of Information and Electronic Engineering
International Hellenic University, Sindos, Thessaloniki, Greece

Abstract— **This research aims to investigate the joint usage of NDVI (Green Normalized Difference Vegetation Index) and LAI (Leaf Area Index) for assessing the crop health and growth conditions of the field. The system includes a Raspberry Pi with a NoIR camera that captures images to be analyzed. GNDVI, mainly used in precision agriculture, involves the estimation of the photosynthetic activity of crops by light reflecting in certain wavelengths. On the other hand, LAI also provides information on leaf area, evaluating the total amount of leaves suitable for plant growth, thus providing further information on the health of the plant. The analysis focuses on evaluating the relationship between these indices and for evaluating specifically how these indices can complement each other in giving the farmer a better assessment of the crop in question. This methodology aims to assist farming practices, focusing on the timing of irrigation, fertilization schedules, and pest control. The results showed that GNDVI and LAI are used for different purposes in crop analysis, while the former measures purely photosynthetic areas, and the latter provides information about vegetation structure and density. In the case of the two indices, the correlation is rather small, nevertheless their simultaneous utilization gives two different perspectives, so the farmer can better manage the crop and make the right decision.**

Index Terms — **Vegetation Indices, Image Analysis, Precision Agriculture, Image Sensor**

I. INTRODUCTION

THE crop health monitoring is a vital part of agriculture sustainability and keeps agriculture in a sustainable manner and using the resources carefully. Vegetation indices such as NDVI (Normalized Difference Vegetation Index) and LAI (Leaf Area Index) are widely employed in photosynthetic activity and leaf area density assessment in the yields. Through these indicators, the farmers are equipped with proper information for making irrigation, fertilization, and crop protection decisions as well as for achieving better resource management and lower production costs [1], [2].

In precision farming, the Normalized Difference Vegetation Index (NDVI) and Leaf Area Index (LAI) are two commonly acknowledged measures of vegetation health. NDVI identifies the degree of vegetation filling up with light energy by differentiation between the reflectance of red and right band light, which is usually from -1 to +1. The strongest, typically green and thick, plants have NDVI values from 0.6 to 0.9 while the stressed or sparse plants are below 0.5. Conversely, LAI is

a measure of plant leaf area density per unit of ground, whereby the greater the leaf area, the better sunlight interception potential. The average value for LAI is crop specific and stage specific but is often from 0.5 to 6 [1]. These indicators bring distinct perspectives to the table, with NDVI picking out places active in photosynthesis and LAI providing information on structural density and biomass distribution of vegetation. Therefore, both indices can be used jointly for assessing crop health and growth with high precision which is an essential component of precision agriculture.

The current day is heavily influenced by UAVs and multispectral sensors. As a result, estimation of large areas of NDVI and LAI parameters has become very easy and rapid. As highlighted by previous studies, these technologies have improved efficiency in taking photographs thereby enhancing the ability to localized performance and enhance productivity [2-6].

Apart from monitoring the greenhouse plants, the employment of NDVI and LAI indices in precision agriculture also contributed to predicting yields and helping to estimate the need for irrigation and fertilization. This allows farmers to manage agricultural resources better, ensuring minimal environmental impact while increasing crop yields.

The technique of NDVI and LAI beyond the simple images can enhance various measurements with resolution and details of images showing various developmental stages of plant growth as well as the demands of the plants. Accordingly, with this model precision agriculture becomes rather affordable and effective by allowing more efficient and accurate evaluation as well as control of crops using fewer resources.

The investigation of NDVI and LAI data shows that it is possible to use modern technologies for precision agriculture and environmental conservation. The combination of these indicators with inexpensive devices, such as the Raspberry Pi, provides farmers and researchers with low-cost means to maximize crop production and cut down on the cost of production [7-9].

Apart from NDVI and LAI, GNDVI (Green Normalized Difference Vegetation Index) also finds increasing acceptance for such purpose for it includes information about chlorophyll content which is not easy to determine by means of NDVI. GNDVI utilizes the green and infrared light channels for comparison offering a better assessment of photosynthetic activity in crops with high chlorophyll content. It has been

established that GNDVI usage can provide an additional broad view on plant status and temporal deeper detection of stress factors contributing to more effective and precise agricultural measures [10].

The calculation of LAI (Leaf Area Index) involves dividing the total one-sided leaf area per unit ground surface area. The formula is written as follows mathematically:

$$LAI = \frac{A_L}{A_G} \qquad (1)$$

where A_L is the total leaf area (m²) and A_G is the ground area (m²).

For GNDVI (Green Normalized Difference Vegetation Index), the formula is:

$$GNDVI = \frac{NIR - G}{NIR + G} \qquad (2)$$

where the NIR is the reflectance in the near-infrared band and the G is the reflectance in the green band. The use of this calculation which contains the green light reflectance, so the chlorophyll content can be highlighted consequently, this also enables the observation of crop photosynthetic efficiency.

The developed crop health monitoring system is a multi-layered modular design using low-cost technologies. At the First Level of Data Collection, NIR and Green light values are recorded using infrared multispectral sensors and high-definition images are captured using NoIR cameras connected to Raspberry Pi devices. The system aggregates data from designated control points on the plot, known as Ground Control Points (GCPs), to achieve spatial alignment and data reliability.

In the Processing and Index Calculation layer the images captured by the NoIR camera are processed on the Raspberry Pi processor using calculation algorithms for the GNDVI and LAI indices. The calculation of GNDVI is based on the relationship between infrared and green spectrum, indicating active photosynthetic activity, while LAI is calculated based on the number of green pixels relative to the ground surface to give an estimate of leaf density.

At the Data Storage and Organization Layer all data is stored in a database organized by date, location and crop type to allow analysis of plant growth. The database includes each measured parameter (eg, GNDVI, LAI) and supports reporting and trending for decision making.
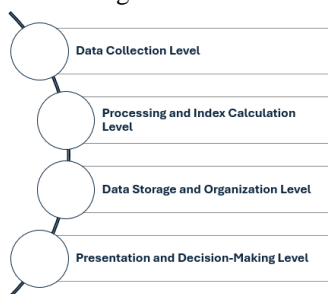

Fig. 1. Schematic description of the system concept.

Finally at the level of Presentation and Decision Making the results of the indicators are presented through a user interface (User Interface), allowing the producers to monitor the health of the crops. The GNDVI and LAI indicators are presented with graphs and maps, offering an immediate view of areas with healthy or problematic growth. This information helps in making decisions about irrigation, fertilization and other farming practices.

The weak correlation between GNDVI and LAI highlights their distinct but complementary roles in assessing the health of certain crops. This approach can reveal novel insights into vegetation dynamics and enhance precision agriculture practices. In specific fields such as GCP 2, a strong linear relationship emerged, indicating that vegetation in these areas follows a more predictable growth pattern. The variability in the GNDVI-LAI relationship between different control points highlights the potential for these indicators to be tailored to suit different agricultural conditions.

II. Experimental Setup

To set up the experiments, a vegetation measurement and monitoring system was implemented by means of a Raspberry Pi with NoIR camera photos of three different fields captured in real-time.

The camera was placed in specific places in the fields at an altitude of 3 meters from the ground with samples taken at ground control points for each field. The experiments performed for each point were repeated 10 times and the values stored are the average values for each size. The images can be stored and transmitted to a central Python server, as well as processed locally or on-site to calculate vegetation indices.
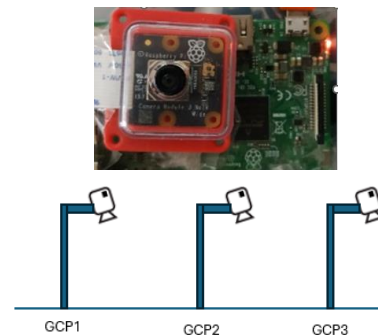
Fig. 2. Experimental Setup

During the experiments, various points within the plot were selected and Ground Control Points were placed for accurate spatial alignment of the images. The data was databased and organized by date, location and crop type, allowing detailed analysis of plant growth.

Along with the image analysis system running in Python, which has been used to control, manage, and analyze the data in real time, the experimental facility has also been set up. The analysis procedure begins with the pre-processing filters that are used for noise removal and the enhancement of images' resolution, and then, the marker estimation algorithms are implemented. This camera technology captures the data that provides the information of the difference in health and growth of the plants with the maximum exactness. The information that has been gathered by this system which shows the differences

in plant health and growth has been monitored with the utmost precision, thus supporting precision agriculture and giving the growers an opportunity to make better-informed decisions regarding their crop management.

III. EXPERIMENTAL RESULTS

This chapter shows the results of the experiments conducted to assess the health and growth of crops by means of the GNDVI and LAI indices. The analysis is based on data collected by the camera, and further processing was executed in Python. The outcome is a real-time estimation of vegetation allowing better agricultural practice decisions.

Sample photo taken with the camera using infrared and blue filters is presented in Figure 3.

Fig. 3. Sample photo with the camera using infrared and blue filter

The infrared (NIR) and green (Green) channels are separated and then processing involves channel normalization and thresholding to separate areas with high photosynthetic activity.

Figure 4 below shows a representative sample of the GNDVI and LAI analysis for the study area. Dark green areas indicate the high GNDVI value, while the corresponding resolution of LAI shows the percentage of foliage per pixel.
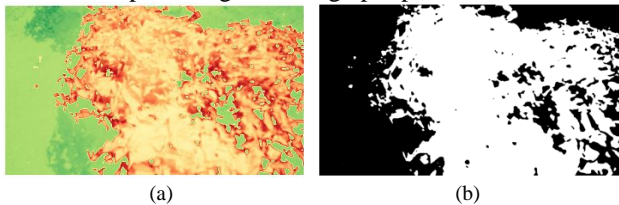

(a)   (b)

Fig. 4. Representative sample of (a) GNDVI and (b) LAI analysis for the study area.

The estimated vegetation percentage is about 38.88%, which falls within a medium level of vegetation health and density in the study area using GNDVI.

LAI was estimated using grayscale analysis of infrared spectrum images and thresholding. This represents the foliage density estimate needed in assessing total biomass and vegetation structure. Using LAI, the estimated percentage of leaf cover was 0.83, with generally relatively sparse vegetation.

The vegetation in this case is completely represented by the comparison between the indices GNDVI and LAI. While GNDVI percentage cover identifies active photosynthetic activity, LAI refers to structural and density features of the vegetation. GNDVI provides early diagnosis on the health status of plants, while LAI gives information on leaf area density and overall growth.

The experimental results reveal that the use of indices like GNDVI and LAI provides practical information to evaluate

crop condition and growth. While the analysis of GNDVI is much more effective in finding areas with high photosynthetic activity, the LAI estimate provides insight into vegetation density in general. Combining both will enhance the chances of more precise crop monitoring and thus provide the basis for improvement in agricultural practice.

The control reference points were used in the experiments and they were placed in different parts of the field. Such an approach provided for the spatial alignment of images and allowed for the temporal comparison of data with satisfactory accuracy. Data captured was filtered, stored into a database, and time stamped. After that, they were organized according to the date, place, and type of crop so that plant growth and health could be analyzed.

Table 1 shows the results of the GNDVI and LAI indices tested on various control points and dates. Day 1 refers to the first day of monitoring, not the initial day of growth.

For every control point, the experimental results are obtained on different dates. The values of GNDVI catch the active photosynthetic activity of the vegetation, while the index LAI gives information on density related to leaf surface.

Table 1. Values of GNDVI and LAI indices at different control points (GCP) and on different dates.

Control Point (GCP)	Date	Average GNDVI	Percent Vegetation Cover (GNDVI)	LAI	Percent Foliage Cover (LAI)
GCP 1	Day 1	0.62	42%	1.2	38%
GCP 1	Day 7	0.68	47%	1.3	41%
GCP 1	Day 14	0.72	52%	1.5	45%
GCP 2	Day 1	0.45	30%	0.9	28%
GCP 2	Day 7	0.50	35%	1.0	32%
GCP 2	Day 14	0.58	39%	1.1	34%
GCP 3	Day 1	0.75	55%	1.5	48%
GCP 3	Day 7	0.78	58%	1.6	50%
GCP 3	Day 14	0.80	60%	1.8	53%

The results at GCP 1 indicate a consistent improvement in vegetation over time, with both GNDVI and LAI showing an upward trend. In contrast, the GCP 2 site exhibits lower GNDVI and LAI values compared to the other sites, suggesting that the vegetation is sparser and there is less photosynthetic activity. GCP 3 stands out with the highest density and cover of vegetation, as evidenced by a GNDVI of 0.80 and an LAI of 1.8 recorded on the final monitoring day.

The differences between the indices on different days and to different points are the fingerprints of the mutual involvement GNDVI and LAI in the offbeat but highly precise detection of crop health, the evaluation of which gives a hint of which areas are under or overgrowth. We can plot a line chart with GNDVI and LAI index changes over time for each control point (GCP) to examine if GNDVI and LAI are complementary in crop health monitoring as shown in Figure 5. Thus, we will be able to ascertain the correspondence of each indicator to botanical growth as well as the differences and similarities between them.
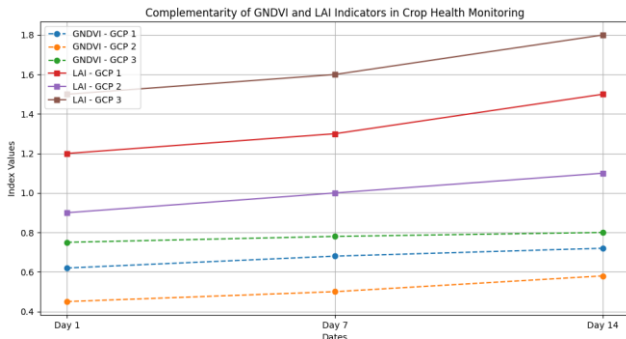
Fig. 5. GNDVI and LAI Indicators in Crop Health Monitoring

The dashed lines are the GNDVI Index, while the solid lines form the LAI index for each control point. This is a much easier way to monitor the change of each indicator alone.

The figure shows that the variations in the two indicators mimic the same pattern but with different intensities, thus they are mutually supportive. The higher index represents greater vegetation.

Figure 6 presents the heatmap demonstrating the mean values of GNDVI for each control point (GCP) on days 1, 7, and 14.
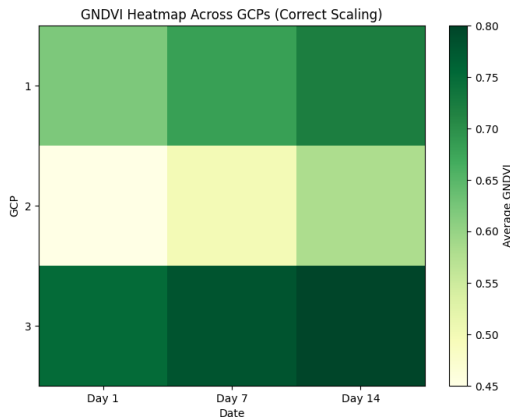

Fig. 6. Heatmap of GNDVI per GCP per days

The higher the number, the healthier the vegetation. The color tones (lighter for low values, darker for high values) easily help to distinguish points of different vegetation health. The increase in GNDVI values at some points, such as GCP 3, demonstrates the improvement of vegetation health over time.
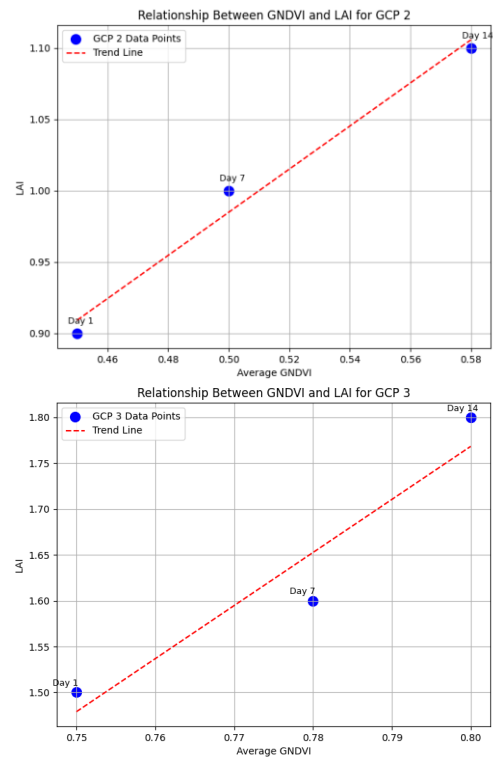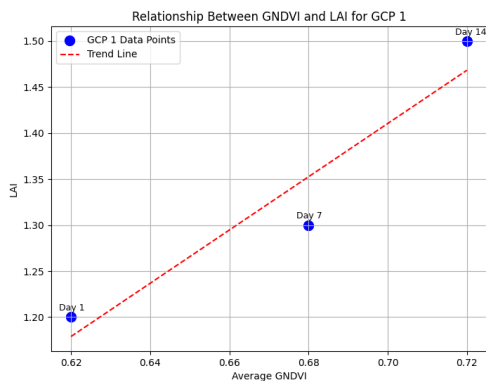

Fig. 7. Plots of relationship between GNDVI and LAI per GCP.

For each GCP chart has been generated with individual trend lines for each of them. The equations and R^2 values are as follows:

GCP 1: $y=2.8947x-0.6158$, $R^2=0.9098$ (3)
GCP 2: $y = 1.5116\,x + 0.2291$, $R^2 = 0.9826$ (4)
GCP 3: $y=5.7895x-2.8632y$, $R^2=0.9098$ (5)

The equations presented here indicate the differences in the GNDVI-LAI relationship for three different control points, which is a clear example of the diversity in the growth parameters and vegetation cover that occurred in the study area. Between these three, GCP 2 is the strongest in the linear relationship having the (R^2) value of 0.9826, thus a very law of close relationship between the GNDVI and LAI. In other words, the vegetation at GCP 2 tends to follow a more predictable growth pattern as compared to the other control points.

IV. Conclusion

This study highlights the significance of GNDVI (Green Normalized Difference Vegetation Index) and LAI (Leaf Area Index) in monitoring crop health and growth, providing cost-effective methods for precision agriculture. The combination of these indicators with low-cost technology such as the Raspberry Pi system with a NoIR camera, has been shown to be successful in the real-time monitoring of the rates of photosynthesis and vegetation density.

The experimental results prove that the GNDVI index is very effective for the capturing of the active photosynthetic activity and thus we are provided with insights into chlorophyll concentration and dynamic plant growth. However, the LAI index provides more details in leaf surface structure and

19

density, thus a quantitative analysis of biomass could be done.

The examination of the relationship between GNDVI and LAI by means of correlation demonstrated a linear dependence, exemplified by a trend line. The data implies that when the GNDVI values, which are the best benchmark for photosynthetic activity, are going up, there is also the corresponding increase in LAI, which means vegetation density and structure. This positive relationship underscores the fact that these two indicators can be used together for more accurate monitoring of crop health and development.

The linear correlation illustrates that GNDVI is better in detecting intense photosynthetic activity, while LAI gives useful information on total biomass. The results of this research are the foundation for the wide use of these indicators in precision agriculture, enabling the timely decision of irrigation, fertilizing, and plant protection.

At the same time, the enhanced machine learning algorithms may enable more sophisticated data analysis in the future. Techniques like deep learning for image analysis or predictive modeling will allow the system to notify the farmers in case of stress conditions and make more accurate yield predictions. These improvements will enable farmers to have better-informed choices and consequently allow them to perfect their practices in precision agriculture.

References

[1] S. Pôças, M. Cunha, M. S. Pereira, J. A. Santos, and L. Pereira, "On the Use of NDVI to Estimate LAI in Field Crops: Implementing a Conversion Equation Library," *Remote Sensing*, vol. 14, no. 15, p. 3554, 2022, doi: 10.3390/rs14153554.

[2] M. S. D. Silva, J. A. P. Ferreira, J. C. A. Costa, and A. M. S. Silva, "LAI Estimation through Remotely Sensed NDVI Following Hail Defoliation in Maize (Zea mays L.) Using Sentinel-2 and UAV Imagery," *Precision Agriculture*, vol. 24, pp. 1–19, 2023, doi: 10.1007/s11119-023-09993-9.

[3] Y. Wang, J. Zhang, X. Li, Q. Wang, and Y. Zhang, "An Optimized Non-Linear Vegetation Index for Estimating Leaf Area Index in Wheat," *Precision Agriculture*, vol. 20, pp. 1–17, 2019, doi: 10.1007/s11119-019-09648-8.

[4] P. Rosso, C. Nendel, N. Gilardi, C. Udroiu, and F. Chlebowski, "Processing of Remote Sensing Information to Retrieve Leaf Area Index in Barley: A Comparison of Methods," *Precision Agriculture*, vol. 23, pp. 1449–1472, 2022, doi: 10.1007/s11119-022-09893-4.

[5] R. Houborg and M. McCabe, "Daily Retrieval of NDVI and LAI at 3 m Resolution via the Fusion of CubeSat and Sentinel-2 Data," *Remote Sensing*, vol. 10, no. 6, p. 890, 2018, doi: 10.3390/rs10060890.

[6] B. D. Wardlow and S. L. Egbert, "Large-area Crop Mapping Using Time-series MODIS NDVI Data: An Assessment for the U.S. Central Great Plains," *Remote Sensing of Environment*, vol. 112, no. 3, pp. 1096–1116, 2008, doi: 10.1016/j.rse.2007.07.019.

[7] G. Zheng and L. M. Moskal, "Retrieving Leaf Area Index (LAI) Using Remote Sensing: Theories, Methods and Sensors," *Sensors*, vol. 9, no. 4, pp. 2719–2745, 2009, doi: 10.3390/s90402719.

[8] J. Kim, Y. Ryu, C. Jiang, and Y. Hwang, "Continuous observation of vegetation canopy dynamics using an integrated low-cost, near-surface remote sensing system," *Agricultural and Forest Meteorology*, vol. 264, pp. 164–177, 2019.

[9] S. Bajocco et al., "On the Use of NDVI to Estimate LAI in Field Crops: Implementing a Conversion Equation Library," *Remote Sensing*, vol. 14, no. 15, p. 3554, 2022, doi: 10.3390/rs14153554.

[10] D. A. García Cárdenas, J. A. Ramón Valencia, D. F. Alzate Velásquez, and J. R. Palacios Gonzalez, "Dynamics of the indices NDVI and GNDVI in a rice growing in its reproduction phase from multi-spectral aerial images taken by drones," in *International Conference of ICT for Adapting Agriculture to Climate Change*, Cham: Springer International Publishing, 2018, pp. 106–119.

The geometry of smart building blocks and its programming

John Nikolaides and Dimitrios Bechtsis
Dept. of Industrial Engineering and Management
International Hellenic University
Sindos, Greece
velona@ahiru.eu

Abstract—**In this paper, we begin investigating how one could build smart building blocks, completely symmetric, that connect to each other both electrically and mechanically. We begin by examining the geometric restrictions that said symmetry would impose on the connectors used. We proceed with a quick description of how the relevant rotations could be efficiently implemented in code. Finally, we examine the necessary further research that would be needed to produce a complete product.**

Index Terms—**play, toys, geometry, symmetry, chiral octahedral symmetry, microcontrollers, embedded**

I. Introduction

We shall begin by stating the assumptions and goals, because those will inform every aspect of our work.

Our goal, then, **is to create childrens' toys** with the following properties:

- **Tesselating,** so as to permit the creation of arbitrary shapes.
- **Symmetric,** so as to ease their use as much as possible.
- **Mechanically Connectible,** to permit the structure to maintain its shape.
- **Electrically Connectible,** to permit data-transfer from one to the other.

The most symmetric 3-D tesselation is the cubic one. We have therefore elected to give our toys cubic shapes. However, this symmetry means that, as our toys get placed and assembled, their orientation will be completely random. Therefore, they must each recognise said orientation, so as to accurately guide the user to place another one "above" or "behind". At the same time, those calculations must be very cheap, so as to permit the usage of cheap hardware.

The goal of the paper, therefore, is two-fold. One, to explore the effects of our choice of symmetry on the cubes' external hardware; two, to present a way to model the cubes' rotations in space in very cheap software.

A. Previous work

Comparable research has been performed by the M-blocks project (cf [1] and [2]). Despite this project's completely different goals, they had to solve much the same problems as we solve in section II, and actually were what convinced us that a solution to said problems is in fact possible. It remains a fact, however, that their work focuses on matters so completely different than ours that our analyses have essentially no overlap.

II. Symmetric placing of connectors

In this paper, we will be making no distinction between electrical and mechanical connectors: anything that pertains to one will also pertain to the other.

One common property of all candidate connectors that we examined is that they all come in complementary pairs, such that they each can only connect with their complementary and not with themselves. To wit: Magnets have north and south poles, stubs need holes in which to fit, electrical pins need electrical pads, and so on. This means that, when placing the connectors on the faces of the cube, we will need to ensure that there is enough space available for both kinds of connector. For ease of visualisation, we will be referring to "red" and "green" connectors, and consider each to be complementary to the other.

With that in mind, let us begin by placing one green connector on one face of the cube, and then examining where the rest of them will end up thanks to our choice of symmetry. We will examine three possible connector placements: One on a diagonal of the face, one on a bimedian, and one placed away from both of those. We will number them 1, 2, and 3 respectively. The result can be found in fig. 1.

We decided earlier that the blocks must be as symmetric as possible. Therefore, each face of the cube must have 4-fold rotational symmetry. We must therefore quadruple the connectors we placed, so that they appear in each vertex of the face. The result can be found in fig. 2.

Thus far, we have only considered green connectors. In order to figure out where the red ones would need to end up, we would need to flip the green ones 180° and place them atop another face. This corresponds to a mirroring, whose output can be seen in fig. 3.

Finally, because each face needs both green and red connectors, we must take both kinds and place them on the same face. The result can be seen in fig. 4.
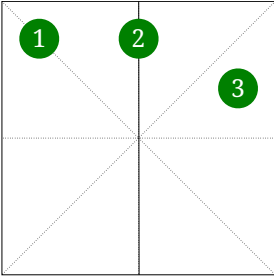
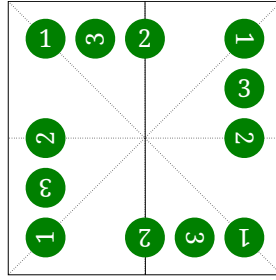Fig. 1: Three possible placements for one connector on one face.

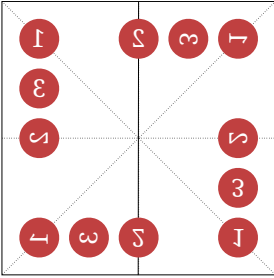Fig. 2: Quadrupling for rotational symmetry.

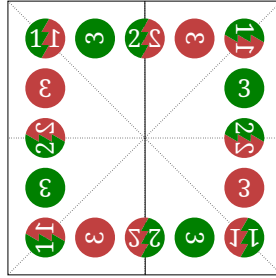Fig. 3: Mirroring for the complementary connectors.

Fig. 4: Conflict between connectors.

This immediately highlights a problem: The connectors that were originally placed on the diagonals or the bimedians end up colliding with their complementary ones. It is only connector placement number 3, which is away from both of those, that fits both kinds of connectors on the face without conflict or asymmetry.

Therefore, the first important geometric restriction we have to contend with is as follows: *No connector can be placed on a face's diagonal or bimedian, because that would force it to collide with its own complementary connector.*

Connector quantities: As we saw on fig. 4, each face of the cube needs (in the general case) 4 red and 4 green connectors. Multiplied by 6 faces, this leads to a total of 24 green and 24 red connectors across the entire cube.

III. The relevant analytic geometry

Having produced a synthetic examination of the relevant restrictions, we can now proceed to describe how said restrictions affect the spatial coördinates of each connector.

Side-note: This sort of symmetry has been quite exhaustively researched, (see for instance [3] or [4],) using terminology such as "chiral octahedral symmetry", "symmetric group", or "discrete point symmetry". This paper will aim to present it using more accessible terminology.

Let there be a cube, centred around the origin, with all its vertices parallel to the axes. Let each of its edges have a length of $2a$, such that all of its vertices are positioned at $[\pm a, \pm a, \pm a]$. Its surface will consist of the points which satisfy $max(|x|, |y|, |z|) = a$.

As we mentioned earlier, none of the connectors can be placed on a face's bimedian or diagonal; therefore, let us examine how those correspond to 3-D space. The bimedians and diagonals are each face's axes of mirror symmetry. Therefore, in order to make the move to 3-D space, we must find the planes of mirror symmetry that the cube's surface has.

Those planes turn out to be nine, in total. Three of them are the three coördinate planes: $x = 0$, $y = 0$, and $z = 0$. Their intersections with the cube's surface produce the faces' bimedians, which means that no connector may be placed on them. As a result, none of the connectors' coördinates may be equal to zero.

The other six planes of symmetry are the diagonal planes, $x = \pm y$, $y = \pm z$, and $z = \pm x$. Their intersections with the cube's surface produce the faces' diagonals, which means –again– that no connectors may be placed on them. As a result of this, none of the connectors' coördinates may be equal to another one's value or its negation. In other words, the coördinates are not permitted to be equal in absolute value[1].

IV. Reflections and Rotations

As we saw earlier, in 2-D space, the placements of the red connectors can be found by mirroring the placements of the green connectors. Therefore, the same must hold in 3-D space: mirroring the placements of the green connectors across one of the cube's planes of symmetry must produce the placement of the red ones. Each one of the cube's planes of symmetry can be used to achieve this, so let us examine the effect that each plane has on a point's coördinates when they are mirrored across it:

5: $x = y$: Swaps the values of the x and y coördinates.

4: $y = z$: Swaps the values of the y and z coördinates.

3: $z = x$: Swaps the values of the z and x coördinates.

2: $x = 0$: Flips the sign of x, ie negates it.

1: $y = 0$: Flips the sign of y, ie negates it.

0: $z = 0$: Flips the sign of z, ie negates it.

(The numbering will be explained in due course.)

Now, the crucial thing to note is as follows: If mirroring the green connectors yields the red ones, then mirroring the red ones must yield the green ones *even if the two mirrorings occur across different planes*. This turns out to be a general geometrical property, which is properly expressed as follows:

Every even amount of reflections (mirrorings) is identical to a rotation. Conversely, every rotation can be decomposed to an even number of reflections.

This means that every possible rotation that can happen to a cube's points can be represented in code as a series of operations on its coördinates: Either swapping the values

---

[1]For reasons which will become apparent later, study of the $x = -y$, $y = -z$, and $z = -x$ will henceforth be omitted as superfluous.

of two coördinates, or negating one of them. The question then arises: How many are needed?

Rearranging the values of coördinates permits a total of 6 possible orderings. Negating each of them or not, in turn, produces 8 possible sign combinations. Multiplying those together yields a total of 48 possible combinations, of which 24 ought to be rotations and 24 ought to be rotations combined with a reflection[2].

The amount of possible rotations can also be found synthetically: Each possible rotation places one possible face on the top (6 possibilities) whose 4 edges can each be brought forward (4 possibilities). Multiplied together, this produces a total of 24 possible rotations, which is consistent with our result above.

V. Efficient representation of points/rotations

We mentioned in II that we need 24 red and 24 green connectors, for a total of 48. But there are also 24 proper and 24 improper rotations, for a total of 48 transformations.

As a result of this, we can establish a one-to-one correspondence between placements and transformations. If we select a specific connector placement as a Point of Reference, then it can be made to coïncide with any other possible placement using just one transformation. This permits us to represent transformations and placements the exact same way: Each placement is represented by the transformation that needs to be applied to the Point of Reference so that it's placed where we want, and each transformation is represented by the place to which the Point of Reference ends up if this transformation is applied to it.

Now, we noted earlier that each of a connector's coördinates must be non-zero and have a unique absolute value. To ease computations, we will elect those absolute values to be equal to $[1, 2, 3]$ respectively; their exact value turns out not to matter one whit, as long as their order is kept consistent.

With all that said, there are 6 possible reflections to be made, listed above in IV. Those will henceforth be called "Elementary Reflections". Also, the fact that we have 48 possible transformations means that a 6-bit integer must be enough to enumerate and represent them. Therefore, we have 6 bits and 6 possible reflections. Thus, the questions that arise are:

- Can the transformations be enumerated in such a way that each bit of the binary representation of the enumeration value corresponds to an Elementary Reflection?
- Can we ascertain that the Elementary Transformations can always be examined in the same order?
- Can we select the enumeration values in such a way that they are contiguous, ie from 0 to 47 inclusive?

[2]Those will henceforth be called "improper rotations", which appears to be the established terminology. In turn, a rotation that can be either proper or improper will be called a "transformation".

The answer to all 3 of those questions appears to be "yes". We achieved this as follows:

- Each bit is ordered according to its number in the list in IV. That is, item number 5 is represented by the bit $2^5 = 32$, item number 3 is represented by the bit $2^3 = 8$, and so on.
- Items number 5 and 4 can never be true at the same time.
- The items are strictly examined in the order $3 \to 4/5 \to 2/1/0$. In other words, item 3 must always be first, followed by items 4 and 5 in either order. Items 0 1 and 2 must always be last, but can be examined in any order.

Obviously, the identity operation will have a numerical representation of 0, and by extension so will the Point of Reference selected.

VI. Programming the rotations

To program the rotations, it suffices to create ways to perform the six Elementary Reflections on the 6-bit integers we analysed above. After that, performing them conditionally (ie depending on each bit of the input) is trivial.

The easiest by far is to program items 2, 1, and 0. In our encoding, "negating the sign" merely means "flipping the bit", which is a very cheap operation. Even better, "flipping this bit if another bit is 1" corresponds to a mere XOR between them. Therefore, items 2 to 0 can be implemented concurrently by a bit-wise AND to isolate their bits, followed by a bit-wise XOR.

As for the other Elementary Reflections, they can be implemented by examining the range in which a given number belongs and conditionally XORing certain relevant bits with a suitable bit-mask. The exact details are rather superfluous, but they can be gleaned by browsing our source-code.

VII. Reciprocals and division

The fact that the bits of each number must be examined in a specific order permits us to ask: What would happen if one were to examine those bits in the reverse order?

The answer is that doing this, and performing the relevant changes to the Point of Reference, will create the reciprocal of a certain rotation—that is, the rotation that does the exact opposite of another one. This permits us to implement division as an operation: the question "What is the rotation we would need to perform on point A so that it would end up coinciding with point B?" can be answered by B/A. This, in turn, can be implemented as $B * A^{-1}$, thanks to the isomorphism between points and rotations. Obviously, $(B/A) * A$ yields A, and AA^{-1} and $A^{-1}A$ both yield the identity operation.

VIII. Creating a Rust library

All the things described in this paper have been used to create a new Rust library, called `cube-rotations`

[5]. The language was chosen for its impressively strict `enum`eration types, as well as its ease in creating test harnesses. Thanks to the former property, it is easy to create a data-type that can only ever take one of 24 or 48 possible values, and to ensure this invariant will never be violated. Thanks to the latter property, it is rather easy to test all our functions exhaustively for correct operation. Together with the `nalgebra` crate, which can describe all the transformations we want in an analytic manner, the crate was tested to 100% certainty of correct operation.

IX. Counting bytes and making Look-Up Tables

When writing programs for very cheap microcontrollers, it is imperative to ensure that the available memories (RAM, program memory, long-term storage) do not overflow. At the same time, using look-up tables (henceforth "LUTs") in order to speed up calculations is very useful, and can even lead to a smaller program at times.

For this reason, we took care to introduce to our `cube-rotations` crate the ability to perform all operations using LUTs. (In the process, this actually let us automatically ensure its correctness.) Two different LUT strategies were used: Small LUTs, wherein each LUT is either 24 or 48 bytes in size, but each operation might consist of more then one look-up; and large LUTs, wherein each operation consists of just one look-up, but each LUT might be up to 576 bytes ($24^2 = 576$) in size.

X. One final note

In the future, it will be useful to permit the faces of our cubes to have small and invisible but important asymmetries. For that reason, it would be beneficial to examine how they could be placed as "symmetrically" as possible, so one face's orientation would immediately yield all other faces' orientations.

To our surprise, this did not end up being an easy thing to do. We were only able to uncover four such arrangements, which are enumerated in figure 5. A brief bibliographic search did not uncover any prior research on the matter, but it appears likely that such research must exist.

XI. Future work

In order to create a more concrete design for the toys we want to create, it will be necessary to answer more questions than the ones we have answered herein. Those include:

- What materials will be used for the construction?
- What sort of electrical and mechanical connectors will be used?
- What circuits will be used internally?
- How will the communication between cubes occur?
- How will it be possible to judge the orientation in which a given cube is found?
- Is it possible to use those smart building blocks in order to guide the player to construct a specific shape?

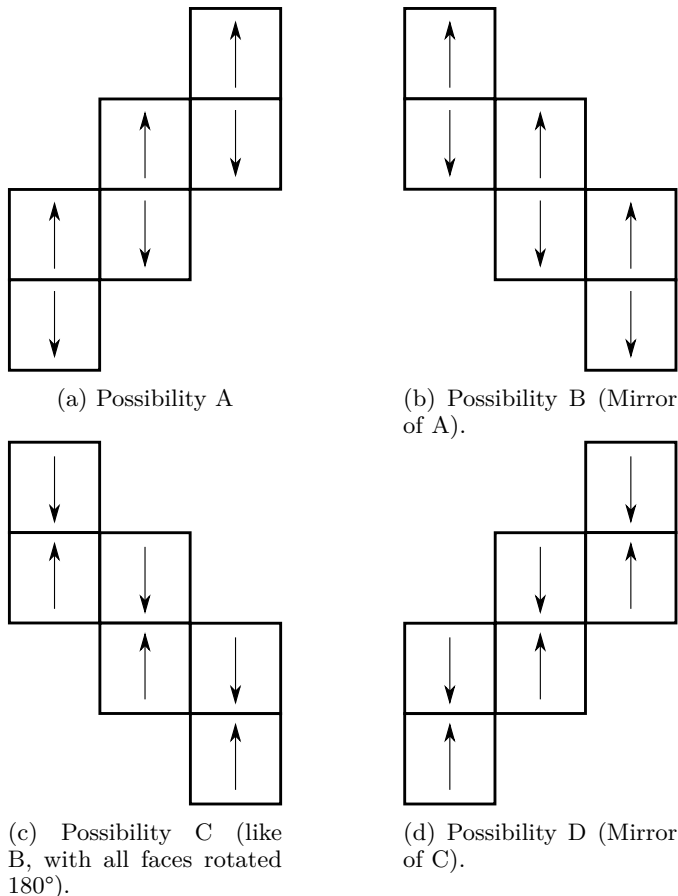Our future work will aim to answer the above questions.

(a) Possibility A

(b) Possibility B (Mirror of A).

(c) Possibility C (like B, with all faces rotated 180°).

(d) Possibility D (Mirror of C).

Fig. 5: The four possible nets with the property described in section X. The arrows denote each face's orientation.

XII. Conclusion

In this paper, we presented the geometric restrictions that must inform the design of the smart building blocks that we aim to build. Firstly, we proved where the connectors can and cannot be placed. Secondly, we produced a way to describe the rotations that can be performed in a program so simple that even the smallest microprocessors can run it. Finally, we enumerated the questions that our future research will need to answer.

References

[1] J. W. Romanishin, K. Gilpin, S. Claici, and D. Rus, "3d m-blocks: Self-reconfiguring robots capable of locomotion via pivoting in three dimensions," in *2015 IEEE International Conference on Robotics and Automation (ICRA)*. IEEE, 2015, pp. 1925–1932.
[2] J. W. Romanishin, K. Gilpin, and D. Rus, "M-blocks: Momentum-driven, magnetic modular robots," in *2013 IEEE/RSJ International Conference on Intelligent Robots and Systems*. IEEE, 2013, pp. 4288–4295.
[3] J. S. Lomont, *Applications of finite groups*. Academic Press, 2014.
[4] H. S. M. Coxeter, *Regular polytopes*. Courier Corporation, 1973.
[5] J. Nikolaides. The `cube-rotations` crate. [Online]. Available: https://docs.rs/cube-rotations/latest/cube_rotations/

Micro-Electro-Mechanical Systems for high frequency implementations (INVITED)

Loukas Michalas

Department of Electrical and Computer Engineering

Democritus University of Thrace, Xanthi, Greece

Institute of Electronic Structure and Laser, Foundation for Research and Technology – Hellas,

Heraklion, Crete, Greece

lmichala@ee.duth.gr

Abstract:

The continues and prompt transmission of the information supported nowadays by implementations in the telecommunication systems, including personal mobile phones and wi-fi networks, has massively affected our everyday lifestyle and its quality. This new reality instigates people to envision novel advances that will enable more futuristic concepts to become real such as those related to the Internet Of Things (IOT) and the satellite communications. These applications require enhanced exploitation of the features of electromagnetic waves and consequently the development of suitable antennas and hardware components referred to as RF (Radio Frequency) electronics. Micro-Electro-Mechanical-Systems for RF applications (RF MEMS) have demonstrated exceptional potential to take over functionalities essential for the realization of these future telecommunication applications like the ability to operate in the upper microwave band frequencies and the capability to effectively deal with the required power burden. This work presents some advances in these domains including the implementation of machine learning and device engineering towards the optimization and the bespoke fabrication of RF MEMS switches with specific characteristics.

Biography:

Loukas Michalas received his Ph.D. in Physics (2009) from the University of Athens, Greece. Since May 2024 he is an Assistant Professor at the department of Electrical and Computer Engineering at Democritus University of Thrace. Previously Loukas was a postdoctoral researcher at the IESL-FORTH (2020-2024), Heraklion, Greece, at the University of Southampton (2016-2019), UK, at the IMM-CNR (2014-2016), Rome, Italy and at the University of Athens (2011-2014), Greece. Over the years Loukas also collaborated via short secondment placements (1-2 months) as visiting researcher with the Keysight Labs (2015), Linz, Austria, with the IEMN-CNRS (2015), Lille, France, with RF Microtech (2021), Perugia, Italy and with Imperial College London (2022), UK. His major research activity is presently focusing on involving machine learning techniques in the development and reliability study of RF nanoelectronics devices and RF MEMS. Parallel research interests include metal-oxide based memristors, thin film semiconductor devices and microwave microscopy. In 2021 Loukas was awarded the competitive Individual Marie Skłodowska-Curie Fellowship grant, whilst presently he is the Principal Investigator in AIMS5.0, a project focuses on using Artificial Intelligence in manufacturing. Apart from research Loukas also enjoys being involved in science outreach activities.
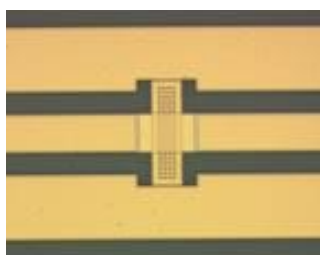
A Bridge type shunt RF MEMS capacitive switch in coplanar waveguide topology

Development of a Data Acquisition and Data Logging Platform

Terzis Vasileios, Nikolaos Tapoglou

Department of Industrial Engineering and Management, International Hellenic University, Thessaloniki, Greece
veh2017053@iem.ihu.gr, vasiterzis@gmail.com

Abstract— **In the context of this work are examined two methods of collecting processing data with the ultimate goal of supporting decision making and creating a historical recording of experimental measurements in a database. The main problem in data acquisition in experimental set up is to monitor the process in the most efficient way possible meaning accuracy in the details. The method of transferring data from the recording device, in our case Raspberry Pi, to the computer via WebSockets communication protocol is also presented as a solution for live display and storage of the measurements of the sensors used. For the effectiveness of the experiments performed, a simplified recording model was created in the recording device. The development of the data acquisition platform and the experimental procedures revealed that the implementation of a DAQ system is influenced by the designer's approach to the specific application and the budget available for its development.**

Keywords— *Process monitoring, Sampling, Raspberry Pi, Python*

I. Introduction

In order to capture all the critical infromation of an engineering process (machining or manufacturing process, experiments ect.) special tools are required with unique characteristics. Data acquisition systems are developed to deliver information about the status of the process which guarantee high precision. A data acquisition system consists of special devices and sensors that are monitoring the process. The remainder of the paper is organized as follows: Section 2 presents the architecture of the DAQ system. Section 3 presents the experimental setup and the results of the experimental trials. Section 4 represents live plotting of temperature data being monitored and transferred by the Websockets communication protocol to the data logging platform from the Raspberry Pi. Finally, Section 5 presents the concluding remarks of the research as well as future work in the field.

II. Data acquisition system (DAQ system) description

To gather experimental data with the Raspberry pi, two models were developed, each offering unique advantages. The first model offers flexibility by monitoring the process remotely using the Raspberry pi as a server and a laptop with the data acquisition platform as a client and communicating via Web-sockets. The second model consists of an individual Python script that reads the accelerometer sensor offering high sampling frequency and it is designed specifically for the main experiment took place in the hydraulics laboratory. Then the data are being transferred to the Data logging platform for plot. An accelerometer and a thermocouple were used to collect crucial information from the experiments. The experimental data have been securely managed in each model chosen for the experiment.

A. Structure of Data logging & acquisition platform

As said above, Raspberry pi is ideal for data acquisition as it features flexibility through its Linux software while offering any kind of modification. Specified features that advance its preference are reading digital signal sensors and communicating through several communication protocols.

The structure of this data acquisition platform offers remote control of sampled data. This huge advantage is achieved throughout a Websocket connection between the Raspberry pi as server and a computer that features the platform as a client. The Raspberry pi acts both as a data acquisition device and a sevrer. A python scipt is constructed that reads both sensors' data and sends them to the client as a struct constuction. Then the Data logging platform unpacks the recieved struct message and implements both save and live plot. This method offers remote supevision of the process using Wi-fi to connect the two IPs.

1) *Raspberry pi and sensors.*

For communication, the I2C (Inter-Integrated Circuit) protocol was selected, valued for its high-frequency data sampling and precision. The clock and data ports facilitate seamless communication between the Raspberry Pi and the sensors. In each model chosen for the experiment, data has been carefully managed to ensure accuracy and security.

Connected sensors have to be connected at least at the following ports: Vin (3.3 or 5 V depending on the sensor), GRN (ground), SDA (data line), SCL (clock line).

Two sensors have been applied for the optimal outcome of the selected experiments as decided were the **ADXL 345 accelerometer** and the **MCP 9600 Type K thermocouple**. Both of the sensors offer analog signal data. This exact compliance had to be made when deciding for the featuring sensors in terms of connectivity (I2C protocol).

2) *Data logging & acquisition platform*

The main concern about the development of the platform was ensuring ease of use for experiments, espcially machining processes, and providing all necessary features for comperhencive experimental monitoring and analysis. Based on this target a Dashbard was created in Python (tkinter GUI) that helps the user interact with monitored data. The main functions that can be operated through the platform are:

• Save experimental metadata such as experiment or process number, machining tool ID, coolant type ect.

• Import constant values of the process that are important for calculations on the experiment. The values are visualized in a log to keep the user up-to-date about the experiment parameters and also saved in the current experiment's database.

• Imported CSV database to plot in different types.

• Import Excel Data from the experimental database which columns can be selected to create an x, y dataset structure.

• Dataset log: a checklist of the imported datasets to plot at any type.

• Different type of plots:

  o Line plot of the imported dataset.

  o Average plot of selected amount of datasets.

  o Standard deviation of the experimental dataset compared to theoretical calculated values.

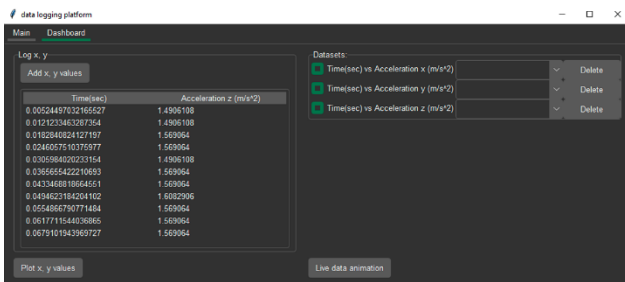 o FFT (Fast Fourier Transformation) analysis of periodical signals.

Fig. 1. Dashboard of the Data logging and acquisition platform.

• Establish a WebSocket connection with the Raspberry Pi to enable real-time data transmission live plotting of sensors' data.
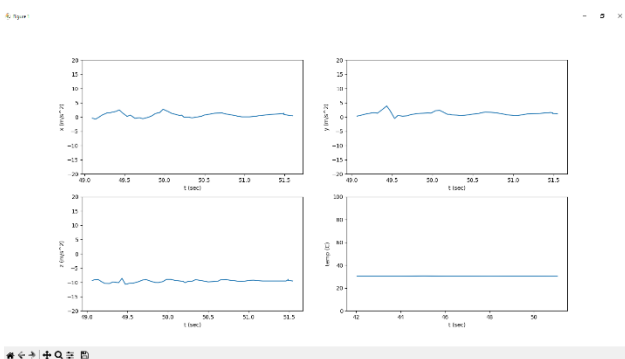

Fig. 2. Flowchart of real time data. a) x acceleration (m/s²), b) y acceleration (m/s²), c) z acceleration (m/s²), d) Temperature (Cº).

B. High sampling rate data acquisition and visualisation method

This model has been used for data acquisition on the experiments took place in this study.

The first part includes a Python script that conducts sampling of the connected sensors with the respective

Python library used for each sensor. Specifically a simple loop is developed to maximize the performance of the Raspberry pi due to high sampling frequency needed for this process. A While True loop continuously reads the accelerometer values and immediately logs them to an Excel database. Once the process completes, the saved data should be transferred to the data logging and acquisition platform for further analysis.

This method of signal monitoring is advantageous due to the simplicity of the functions taking place.

C. Important consideration

Setting up the parameters of the data acquisition system requires considering both the sampling frequency needed for the experiment and the capabilities of the devices avaliable. It is essentially a balance between the experiment's requirements and available resources.

In this study the frequency needed to be applied to the accelerometer was verified by the Nyquist theorem. Nyquist stated that to accurately capture a periodic phenomenon without aliasing, the sampling rate must be at least twice the highest frequency of the signal. The maximum frequency that can be monitored is known as the Nyquist frequency
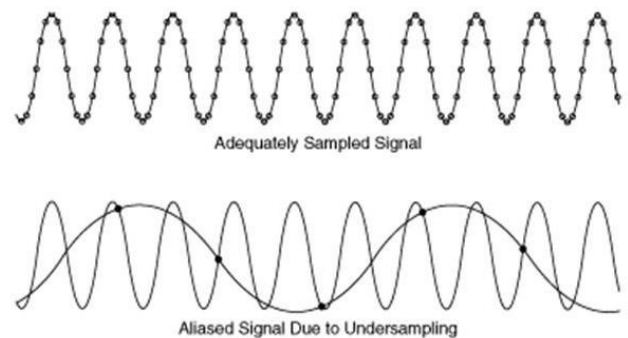

Fig. 3. Graphical explanation of a perfectly sampled signal compared to aliasing phenomenon. *(Source:* [1]*)*

$$f_{sample} \leq 2 \times f_{monitoring}$$

For better signal monitoring many modern researches utilize 5-10 times greater sampling rate [2]. Although it is preferred to monitor in such high frequencies, the efficiency and limitations of the monitoring devices and sensors must also be considered.

III. EXPERIMENT IN THE PNEUMATICS AND HYDRAULICS LABORATORY

An experiment was conducted in the Pneumatics and Hydraulics systems laboratory of the Department of Industrial Engineering and Management to measure the displacement rate of an air compressor. The experiment aimed to validate the DAQ system's performance and ensure the accuracy of the measurements. The target was to monitor the vibrations of the air compressor with the ADXL 345 accelerometer being placed in the crankshaft's case of the compressor.

2

Fig. 4.   Air compressor of the experiment.

To set the monitoring frequency at a satisfactory level it was needed to calculate the frequency of the compressor. This has been achieved by calculating the compressor frequency from the nominal rotation frequency of the motor 2750 rpm (As per the manufacturer's specification). The pulley diameters of the motor and the air compressor are 13cm and 28 cm respectively.

$$f_{motor} = \frac{2750}{60}$$

$$f_{compressor} = \frac{D_{motor}}{D_{compressor}} \times f_{motor}$$

$$f_{compressor} = \frac{13}{28} \times 45.833$$

$$f_{compressor} = 21.2 \; Hz$$

Given the compressor's frequency the sampling frequency has been set to 200 Hz (Sampling interval: 0.005 sec), which is nearly ten times higher than the air compressor's frequency of 21.2 Hz.The simplified data acquisition method has been used to achieve this high frequency sampling.

The experiment is split to three phases. In each phase the tank is filled with air causing changes in the internal pressure. The purpose is to monitor the process closely and identify any deviations using the developed DAQ system.

A. First phase (filling of 0-2 bar)

In the first phase of the experiment the compressor starts to fill the tank which is complitely empty on purpose. The process took time of 79.4 seconds. Speculating the accelerometer data visualised by the Data logging platform can be clear that the data recorded from this first phase come out with a little of noise.
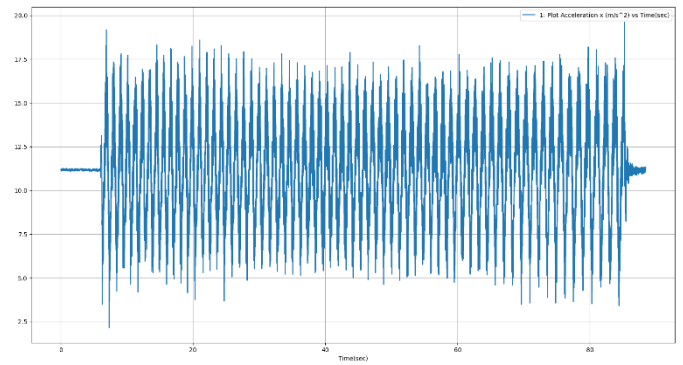

Fig. 5.   First phase accelerometer data. *(Source: Data logging & acquisition platform)*

This becomes more clear when FFT analysis is performed on the accelerometer data. The peak frequency stands out at 21.6 Hz which is the compressor's operating frequency as it shown on the calculations. The respective frequency of the motor is shown as a peak at 45.7 Hz.
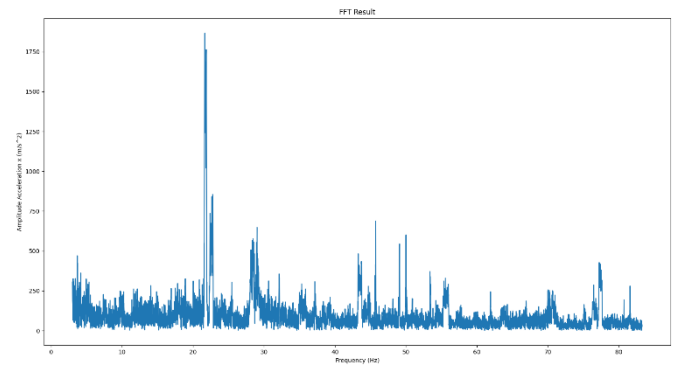

Fig. 6.   First phase FFT analysis. *(Source: Data logging & acquisition platform)*

B. Second phase (filling of 5-7 bar)

At the second phase of the experiment no significant differences have been observed. The second phase took 105.7 seconds to complete which is normally higher from the first period of time.
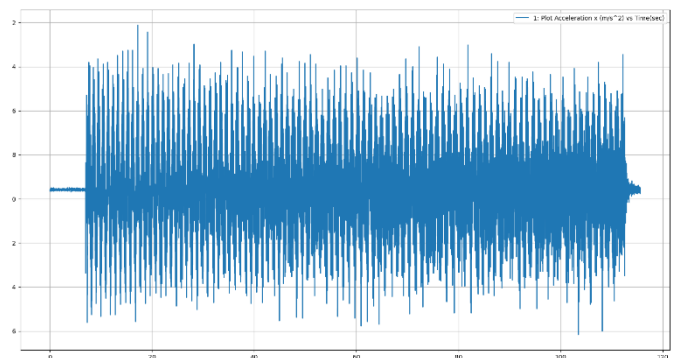

Fig. 7.   Second phase accelerometer data. *(Source: Data logging & acquisition platform)*

FFT analysis of the accelerometer data revealed the compressor's operating frequency to be 21.3 Hz, which remained relatively stable throughout the second phase.
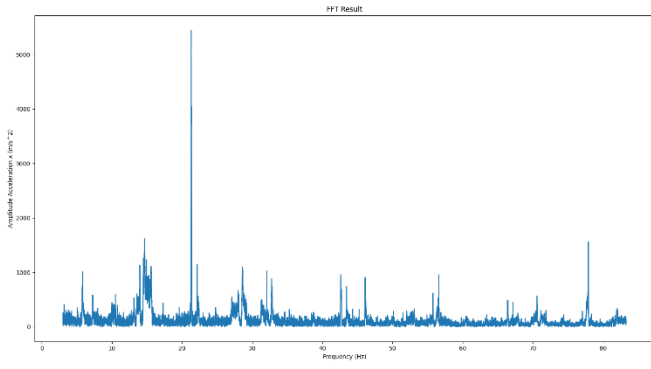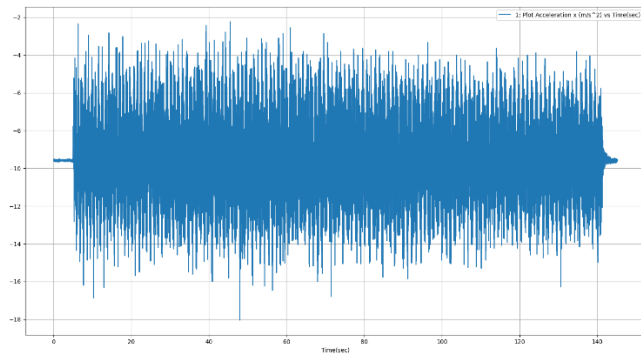
3

Fig. 8.   Second phase FFT analysis. *(Source: Data logging & acquisition platform)*

C. Third phase (fillIng of 7-9 bar)

In the third phase, the operating temperature was significantly higher, introducing considerable noise in the accelerometer data due to the increased difficulty of overcoming the tank's pressure. This phase also took longer than the previous two, requiring 136 seconds to reach full capacity.
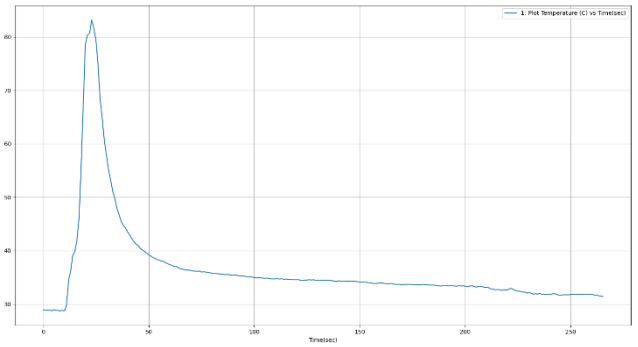

Fig. 9.   Third phase accelerometer data. *(Source: Data logging & acquisition platform)*

The FFT analysis of the last phase shows more abrupt peaks than the other two graphs caused from the increased volume of data. The compressor's operating frequency has been slightly reduced at 21.2 Hz while the motor peak is shown at 43 Hz.
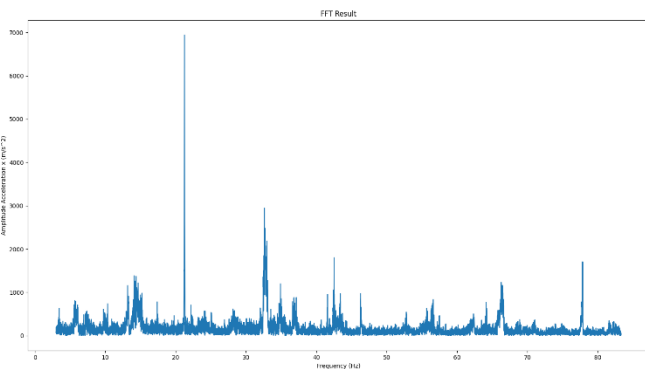

Fig. 10. Third phase FFT analysis. *(Source: Data logging & acquisition platform)*

IV. TEMPERATURE MONITORING

To check the reliability of the DAQ's indirect monitoring method in live circumstances a simple experiment took place. A drill positioned verticaly on a wooden piece made a small hole while the temperature was monitored from the thermocouple sensor placed near 4 mm of the processing area and plotted live into the Data logging & acquisition platform.

Fig. 11. Real time temperature monitoring. *(Source: Data logging & acquisition platform)*

V. CONCLUSIONS

After investigating all the accelerometer data and the respective FFTs of all the phases of the experiment the conclusions are clear. Although the sampling rate was set at 200 Hz the peak frequency on the FFT diagrams was 83.2 Hz which is the Nyquist frequency. Although this does not impact the quality of the monitored sample, it is likely due to the slower processing time of the recording device compared to the specified sampling interval of 0.005 seconds. This issue has been addressed on the respective recording time of each phase of the experiment and the measurements where 16.7% lower than expected compared to the sampling frequency set on the DAQ. For example the actual amount of measurements that the DAQ saved was 24,183 for the respective time of 145,177744 seconds. The expected amount of measurements at the same period of time for 200 Hz sampling rate are 29.035. While the deviation remained constant in all the experimental phases it is clear that the issue was the process power of the Raspberry pi and does not affect the quality of the frequencies that are being examined in the experiment.

Looking at the experiment results it has been observed that the filling rate decreases as the tank's pressure increases.

TABLE I.   EXPERIMENT RESULTS.

Phase:	1	2	3
Time (sec)	79,42	105,74	136,17
Filling rate (bar/min)	1,506	1,134	0,881
$f_{compressor}$ (Hz)	21,66	21,3	21,25
f_{motor} (Hz)	45,75	43,44	43,39

The research on DAQ systems and the development of the data logging and acquisition platform resulted in an effective experimental model. Beyond its current applications, this model has the potential to evolve into a machine learning tool for optimizing machining processes, such as predicting tool wear.

4

REFERENCES

[1]   K. K. Agguna, "Vibration signal processing (sampling & Aliasing)," *Linked in,* 2019.

[2]   M. I. M. I. S. A. A. &. J. N. a. A. Zurrayen, "Evaluation of Tool Wear and Machining Performance by Analyzing Vibration Signal in Friction Drilling," *ResearchGate,* 2020.

[3]   *Understanding the discrete fourier transform and the FFT.* [Film]. MATLAB, 2024.

[4]   B. T. F. S. T. L. A. Z. M. &. V. A. Schmucker, " Implementation of an intelligent system architecture for process monitoring of machine tools.," *Procedia CIRP,* p. 5, 2021.

[5]   P. P. A. &. S. T. Stavropoulos, "Indirect online tool wear monitoring and model-based identification of process-related signal," *Advances in Mechanical Engineering,* 2020.

[6]   G. M.-A. G. B. P. &. R. S. Terrazas, "Online Tool Wear Classification during Dry Machining Using Real Time Cutting Force Measurements and a CNN Approach," *Journal of Manufacturing and Materials Processing,* 2018.

5

Acoustic Power Transfer Through Solid Surfaces

Ippokratis Kochliaridis and Michail E. Kiziroglou
International Hellenic University, Greece

Recently, many wireless interfaces have been developed for communication and power transfer of isolated or hermetically sealed sensors and without the need of batteries for operation [1]. However, each technology has benefits and disadvantages. For example, RFID which is based on electromagnetic signals, couldn't penetrate metallic surfaces due to faraday shielding effect or is limited to a very low bandwidth [2]. Acoustic Power Transfer (APT) however, uses mechanical waves to transmit signal from a point to another. In general, an APT system consists of 3 main electroacoustic stages (transmitter, medium and receiver part as is shown in figure 1. Top). Most of APT systems use piezoelectric transducers with ultrasound frequency response, usually at frequencies between tens of KHz and 1 MHz [3]. The transmitter uses the piezoelectric effect to generate mechanical waves from electrical signal. Accordingly, the receiver converts mechanical waves to electrical power using piezoelectric effect again [4] (Figure 1. Middle represents the Mason modelling circuit for the three electroacoustic stages). The type of medium varies and depends on application. However, some APT systems with ultrasound transducers utilise metal surface, because the acoustic/electrical impedance of piezoelectric element, matches better with the acoustic impedance of metal. Thus, the overall efficiency of power transfer is increased [3][5]. There are mission critical applications, where monitoring sensors are remotely positioned, such as: sonar systems, submarine etc [6]. In that case drilling isn't a preferable solution due to luck of mechanical strength and water leakage. Thus, an APT based on mechanical waves transmitted across a metallic surface, is a recommended solution for above applications (Figure 1. Bottom).
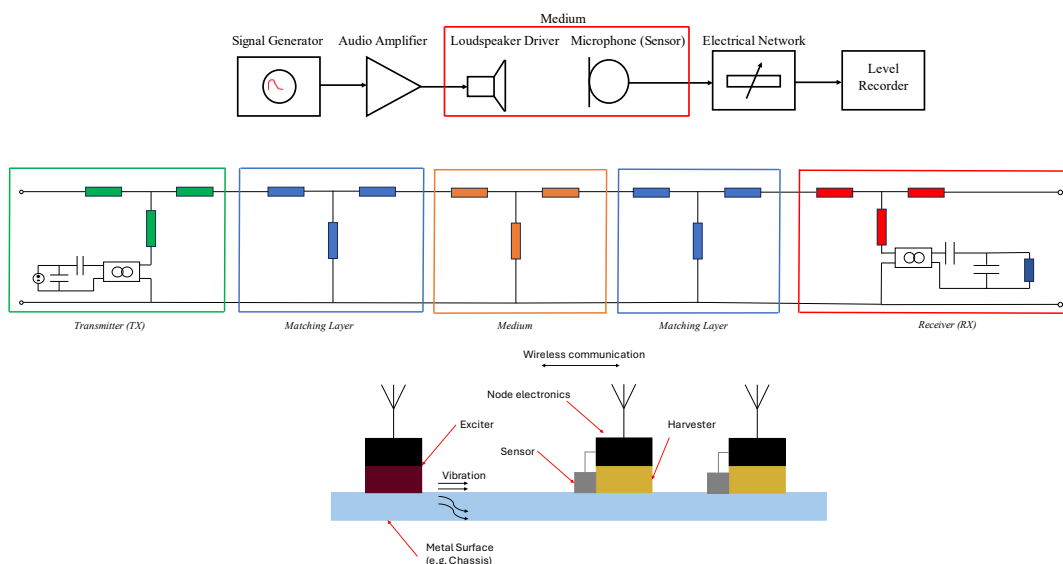

Figure 1. Left: The block diagram which describes the APT concept. Middle: The equivalent electrical circuit of the Mason's model for an APT based on piezoelectric elements. Right: An APT system suitable for marine applications.

References

[1]   Yang et al, "Through-Metal-Wall Power Delivery and Data Transmission for Enclosed Sensors: A Review", Sensors, 15, 31581, 2015
[2]   Freychet et al 2020 eng. "Analytical optimization of piezoelectric acoustic power transfer systems" Eng. Res. Express 2 2020 045022.
[3]   Yang et al, "An Ultrasonic Through-Metal-Wall Power Transfer System with Regulated DC Output" Appl. Sci., 8, 692, 2018
[4]   Sung Q Lee, Woosub Youm and Gunn Hwang "Biocompatible wireless power transferring based on ultrasonic resonance devices" 2013 Acoustical Society of America, Received 22 Jan 2013; published 2 Jun 2013.
[5]   Du G, Zhu Z, Gong X "Fundamentals of Acoustics 3rd ed" Nanjing University Press: Nanjing, China, pp, 351-352, 2012
[6]   BAE Systems. Walls Have Ears—The Technology that Can Communicate Electronically through Solid Steel. http://www.baesystes.com/Newsroom/NewsReleases/autoGen110618172929.html, (accessed on 27 August 2010).

Emerging Technologies for Effective Humanitarian Crisis Management

Anastasios Ntabizas[1], Maria Drakaki[1] Panagiotis Tzionas[2]

[1] Department of Science and Technology, International Hellenic University, 14th km Thessaloniki-N. Moudania, 57001, Thermi, Greece

[2] Department of Industrial Engineering and Management, International Hellenic University, PO BOX 141, 57400, Thessaloniki, Greece

Abstract - **Humanitarian crises require innovative approaches to enhance and support their management. This paper explores how emerging technologies like data analytics, AI, and early warnings systems (EWS) enhance crisis response through improved decision-making, resource allocation, and coordination. Case studies such as the flood management in South Asia, tsunami alerts by UNESCO-IOC and "early warning for all" initiative illustrate their impact. Ethical concerns such as data privacy and AI bias are addressed, emphasizing robust frameworks. Future innovations in blockchain and drones highlight the need for responsible and collaborative solutions.**

Keywords- Crisis management, humanitarian technologies, artificial intelligence, blockchain, drones, ethical considerations.

I. INTRODUCTION

Humanitarian crises, ranging from natural disasters to armed conflicts and pandemics, have become increasingly complex. Rapid technological advancements offer tools to address these challenges more effectively. Technologies such as AI, data analytics, and digital communication are revolutionizing crisis response, enhancing situational awareness, and facilitating better decision-making. Similarly, Early Warning Systems (EWS) have emerged as critical tools in mitigating the impacts of disasters. By integrating hazard monitoring, forecasting, and timely dissemination of warnings, EWS enable proactive measures to reduce loss of life and property. However, the integration of these technologies must be align with humanitarian principles, considering ethical challenges like data privacy and algorithmic biases, and equitable access to warning systems. Ethical guidelines and risk assessments are critical to ensuring responsible technology deployment [1] and effective solutions like EWS in reaching vulnerable communities.

II. HUMANITARIAN CRISIS MANAGEMENT TECHNOLOGIES

Recent advancements are reshaping how crises are managed. Key technologies include:

- Data Analytics: Provides real-time insights for identifying vulnerable populations, predicting crisis hotspots, and allocating resources efficiently.
- Artificial Intelligence (AI) and Machine Learning (ML): Supports predictive modeling, enabling proactive responses, optimizing resource distribution, and aiding logistics planning.
- Communication Technologies: Tools such as mobile apps, satellite networks, and digital platforms improve information dissemination, enabling rapid coordination among responders.

III. CASE STUDIES AND APPLICATIONS OF EWS

Early Warning Systems (EWS): Technologies used to detect and predict hazards such as floods, tsunamis, earthquakes, and health emergencies. These systems typically combine various data sources, such as satellite monitoring, weather stations, and predictive models, to assess risks and issue warnings. An effective end-to-end EWS includes four core elements, where each must function efficiently for the system to be successful:

1. **Risk Knowledge**: Building a baseline understanding of risks (hazards and vulnerabilities) and priorities at a given level.
2. **Monitoring**: Keeping up-to-date on how those risks and vulnerabilities change over time.
3. **Response Capability**: Reducing risk once trends are spotted and announced, whether through pre-season mitigation activities, evacuation, or duck-and-cover reflexes, depending on the warning lead time.
4. **Warning Communication**: Packaging monitoring information into actionable messages understood by those who need, and are prepared, to act upon them.

EWS integrates gathering, processing, and presenting information to generate alert messages and transmits these to citizens at risk through effective warning communication [6]

Flood Management in South Asia: Advanced EWS have been implemented across South Asia to monitor hydro meteorological events such as floods and cyclones. Utilizing satellite-based technologies for real-time data, governments have improved forecasting accuracy and targeted response efforts. These systems combine Earth observation data with in-situ measurements to provide actionable insights, enabling communities to evacuate in time [2].

Tsunami Alerts by UNESCO-IOC: Since the 1960s, UNESCO's Intergovernmental Oceanographic Commission has developed tsunami EWS in oceans like the Pacific and Indian Oceans [3]. These systems leverage seismic monitoring and oceanic buoys to detect tsunamis and issue warnings within minutes, enabling governments to execute rapid evacuation measures.

"Early Warnings for All" Initiative: Launched in 2022 by the United Nations Office for Disaster Risk Reduction (UNDRR) and the World Meteorological Organization, this initiative aims to provide inclusive, multi-hazard EWS coverage globally by 2027. It employs space-based technologies, including satellite imagery and Global Navigation Satellite Systems (GNSS), to enhance preparedness and resilience[4] [5].

IV. ETHICAL CONSIDERATIONS

While technology enhances crisis management, ethical concerns must be addressed:

- Data Privacy: Collection and use of sensitive data necessitate strict privacy controls.
- AI Biases: Algorithms must be carefully designed to avoid reinforcing biases.
- Surveillance Risks: Monitoring technologies must respect individual rights and freedoms.

Developing ethical frameworks and conducting risk assessments can ensure that technological advancements uphold humanitarian values.

V. CONCLUSION AND FUTURE DIRECTIONS

As crises grow in scope and complexity, leveraging technology becomes indispensable. Emerging tools like blockchain and drones show promise in enhancing efficiency, transparency, and coordination. However, ethical challenges must be prioritized to foster trust and ensure responsible innovation.

Example applications of EWS include:

- **Global Wildfire Information System (GWIS)**: A joint initiative of GEO and Copernicus, GWIS integrates regional and national fire data to provide a comprehensive global view. It offers tools for operational wildfire management, country profiles, and downloadable data on fire regimes, burnt areas, and land cover damage [7].
- **Global Drought Information System (GDIS)**: Operated by NOAA, GDIS provides tools for visualizing drought data and resources for forecasting and managing drought conditions. These systems combine archived and up-to-date satellite imagery to enhance early warning efforts [8].

Future efforts should focus on:

1. Strengthening global collaboration to develop standardized frameworks.
2. Integrating human decision-making with AI capabilities.
3. Expanding the use of emerging technologies in disaster prevention and recovery.

By fostering multidisciplinary collaboration and prioritizing ethical considerations, technology can play a transformative role in mitigating the impact of future crises.

REFERENCES

[1] Tzachor, A., Whittlestone, J., Sundaram, L. *et al.* Artificial intelligence in a crisis needs ethics with urgency. *Nat Mach Intell* **2**, 365–366 (2020). https://doi.org/10.1038/s42256-020-0195-0

[2] UN-SPIDER Knowledge Portal, "Early Warning Systems," Available at: https://www.un-spider.org/risks-and-disasters/early-warning-systems#no-back (accessed 10 November 2024).

[3] UNESCO-IOC, "Tsunami Early Warning Systems," Available at: https://ioc.unesco.org/ (accessed 10 November 2024).

[4] UN-SPIDER Knowledge Portal, "Early Warnings for All Initiative," Available at: https://www.un-spider.org/node/13388 (accessed 10 November 2024).

[5] UN-SPIDER Knowledge Portal, "Space Technologies for Early Warning Systems," Available at: https://www.un-spider.org (accessed 10 November 2024).

[6] PrepareCenter.org, "Early Warning Systems," Available at: https://preparecenter.org/topic/early-warning-systems/ (accessed 10 November 2024).

[7] Global Wildfire Information System (GWIS), "Applications," Available at: https://gwis.jrc.ec.europa.eu/ (accessed 10 November 2024).

[8] Global Drought Information System (GDIS), "Drought Information," Available at: https://gdis-noaa.hub.arcgis.com/ (accessed 10 November 2024).

Development of a data acquisition system for underwater environmental measurements

Afroditi Antoniadou, Theodoros Kosmanis[0000−0002−8730−1345] and Dimitrios Tziourtzioumis[0000−0002−1881−3953]

Laboratory of Energy Systems, International Hellenic University, Alexander University Campus, 57400, Sindos, Greece

afroditeanton@yahoo.gr

Abstract— **This research aims to study, design and implement a sensor system for measuring water quality parameters in aquatic environments. The need for real-time water monitoring has increased significantly, as water pollution is a major issue and has direct impact on the ecosystem and human health. The study focuses on the use of technology as Internet of Things (IoT), which allows the collection and analysis of environmental data from various sensors. The methodology follows the development of a sensor system that can measure physical water parameters such as hydrogen potential (pH), electrical conductivity (EC), oxidation-reduction potential (ORP) and dissolved oxygen (DO). These sensors are connected to a Raspberry Pi microcontroller, which collects the measurements and transmits them to a computer for further analysis. The experimental operation of the system was carried out in natural aquatic environments in the Thermaikos Gulf region to tests its efficiency and reliability. The results showed that the system can provide reliable and continuous measurements, offering a framework for evaluation of water quality and aquatic life conditions. It is demonstrated that a low-cost water monitoring system based on sensors and IoT applications has the potential to contribute significantly to the evaluation and preservation of aquatic environment.**

Keywords—**Environmental Measurements, IoT, Real-time water monitoring, Low-cost monitoring system**

I. INTRODUCTION

WATER is one of the most essential resources for the maintenance of all species on the planet, including humans [1]. In recent years, water pollution has been identified as a major issue as it is directly related to the quality of drinking water. [2] To address this situation, the Internet of Things (IoT) and its applications are here to give an innovative solution.

Today, the concept of IoT is a phenomenon which has improved various sectors worldwide. Sensors have a significant role in these applications as they are able to detect physical or chemical changes and collect the data, automating some applications. [3] The first sensor that was effectively suitable for monitoring was the glass pH electrode, which in its current form was developed around 1930. Since then, the measurement of hydrogen potential (pH) has become a fundamental parameter for most water monitoring devices. However, it is clearly necessary to measure more water parameters to draw conclusions and this can be obtained by implementing systems consisting of a group of sensors. [4]

In the past, water quality monitoring involved collecting samples and carrying out laboratory tests to assess the water quality. Nowadays, the need for real-time water monitoring has become critical and this has led to the development of low-cost systems that can provide the required information. [5,6] By integrating these sensors with a low-cost microcontroller, such as a Raspberry Pi, this research aims to develop an efficient and cost-effective system for monitoring aquatic environments. According to the above, the purpose of this paper is to design and, implement and testing of a sensor-based monitoring system for assessing water quality in natural aquatic environments, specifically within the Gulf of Thermaikos.

II. MEASURING EQUIPMENT

To develop a reliable water quality monitoring system, this study uses specialized measurement equipment that includes a variety of sensors and a Raspberry Pi microcontroller. These components work together to provide real – time data on critical water parameters. (Fig.1).

A. Sensors

The sensors selected involved three (3) parts. The first one has the capability of simultaneous measurements of pH,
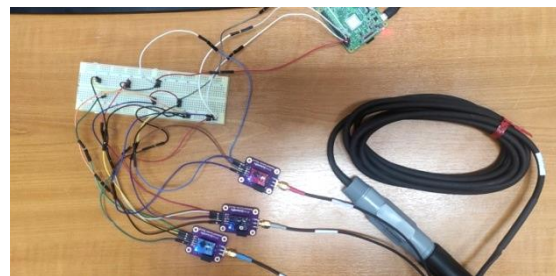

Fig. 1 pH, ORP and Temperature sensor connected to Raspberry Pi

ORP and Temperature. The second one implements measurements for conductivity and through this, parameter values for Total Dissolved Solids (TDS), salinity and specific gravity (which is only applicable in sea water) are calculated. Finally, the third one implements

measurements for the amount of dissolved oxygen (DO) present in the water.These parameters have the advantage of being easier and faster to be measured than others. [7] The explanation and the typical values for sea water environments are given in detail below.

pH determines how acidic or alkaline water is in range from 0 to 14, with 7 being neutral. Values less than 7 indicate acidity while values greater that 7 indicate alkalinity. The average pH of seawater is 7 to 8.5, meaning basic or alkaline.

Conductivity (EC) defines the ability of water to conduct electricity, which is determined by the concentration of dissolved ions. High values correspond to higher levels of ion concentration. Conductivity is also closely related to Total Dissolved Solids (TDS), which represent the concentration of dissolved substances in water. Also, salinity of water that can be estimated, is important for the health of marine organisms. Finally, specific gravity is extracted from EC, indicating the density of seawater in relation to pure water. The latter is affected by the dissolved ion content. The average conductivity of fresh surface water is between 5000 and 30000 µS/cm.

ORP measures the ability of water to release or accept electrons during chemical reactions, indicating its oxidization or reduced capacity. High values means that water is safe (non polluted) as it can effectively break down contaminants. Typical values are between 200 mV and 400 mV.

Dissolved oxygen (DO) measures the amount of atmospheric oxygen dissolved in water, which is essential for the respiration of aquatic organisms. Low levels of dissolved oxygen can cause uncomfortable conditions for aquatic life and disrupt the ecosystem. The concentration of dissolved oxygen in seawater is typically 7 to 8 milligrams per litre (mg/l). Dissolved oxygen varies significantly with temperature, pressure and salinity.

Temperature has the ability to influence the rate of chemical reactions and biological processes, as well as the metabolic rate of aquatic organisms. Sudden changes in temperature can affect marine organisms. Temperature in sea water decreases gradually with increasing depth.

B. Raspberry Pi microcontroller

A microcontroller is needed to operate the sensors and read their data. The microcontroller is the communication link between the sensors and the user. Essentially, the sensors are wired to the microcontroller and the user inserts the appropriate command code into module environment in order to receive the sensor data.In this proposed system, Raspberry Pi Model B was used. In fact, microcontroller has forty pins, which can support the connection of cables for any application.

III. RESULTS

For the assembly of the proposed system, the experimental procedure involved the following steps. First, the Raspberry Pi 4B was configured to recognize and communicate with the sensors via communication protocol. This was done with a series of commands through the Raspberry Pi sample code manual from the manufacturer. In this application, the I2C communication protocol was used. The next step was to connect the sensors to the Raspberry Pi and verify that they communicate with the microcontroller, according to the default protocol positions. [8]

After the sensor communication control was completed, the sensors were able to be calibrated. The sensors were calibrated by a specific procedure defined by the manufacturer using appropriate chemical solutions. The sensors were placed in the solutions and their control software was configured to read each sample at an appropriate value. Ultimately, all sensors demonstrated the capacity to measure within their respective ranges.

In order to implement the sensor measurements and to collect and process data efficiently, a custom code was created in the Python programming language. This code consists of two parts called server and client, in aim to achieve communication between the Raspberry Pi and the sensors. The server part is executed on the microcontroller and is responsible for managing communication with the sensors and the client part is responsible for the visualization of the measurements in a control panel and storage them in a CSV file. In this way, the development of a low-cost system for the monitoring of environmental parameters of water using the applications of the Internet of Things (IoT) for the acquisition and collection of data was completed and measurements were carried out in the coastal areas of Halastra and Nea Michaniona in Thessaloniki, Greece.

A. Measurements in Halastra

The first set of measurements took place in the area of Halastra in Thessaloniki on 6th June 2024. This place is a mussel cultivation zone, one of the most important shellfish cultivation centers in Greece.[9] (Fig. 3)
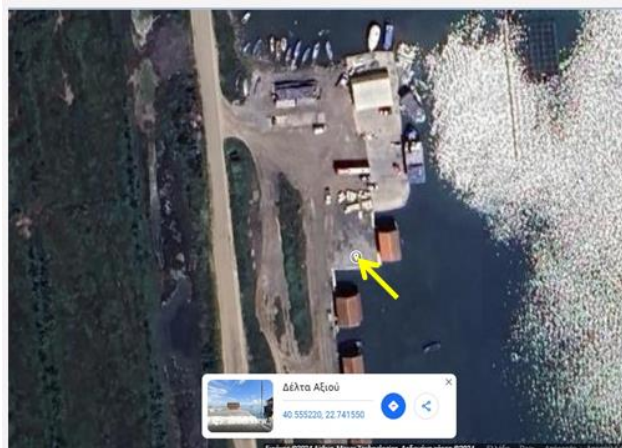

Fig. 2 Measurements point in Halastra, Thessaloniki, Greece

After achieving the appropriate connections of equipment, measurements were made using each sensor

separately and the data were stored locally. The process was turned successful for the sensors of pH, ORP, temperature and EC. Data sampling rate for each sensor was about 0.7Hz and the process was stopped when the data received were stabilized, something usually occurred within a few minutes. The limitations of the process were correlated with the distance from the shore and depth of the water. Due to the manual submerging of the sensors in the water, the coverage distance was the closest to the shore and depth approached by each sensor was about 1m. However, possible obstacles that might be present were not visible due to the turbidity of the water. According to Table 1, the results show that the aquatic environment in the area of Halastra is not suitable for the growth of mussels. The presence of microorganisms and pollutants, as well as the conditions of low salinity and high temperature are not suitable for this environment, even with the existence of balanced values of conductivity and total dissolved solids.

Table I. Measurements of aquatic environment of Halastra

Sensor Type	Values
pH	9.06
ORP (mV)	142.44
EC (μS/cm)	5868.64
TDS (ppm)	3169.32
Salinity (ppt)	3.18
Specific Gravity	1.003
Temperature (ºC)	30.26

B. Measurements in Nea Michaniona

The second set of measurements took place in the area of Nea Michaniona in Thessaloniki on the 26th September 2024. It is also an important fishing center for fish and shellfish. [10] The measurements carried out at three points in the marine of Nea Michaniona. The first point focused on the front side of the marine where the boats are moored. The second and third points focused on the back side of the marine, where measurements were taken at the pier head and berth of the marine, where bigger boats are moored. The procedure that was followed was the same as it was in Halastra area.

This time, the process was successfully completed for all sensors, including the DO sensor, which provided measurements without any problems. According to the Table 2, most of the key water parameters indicate that the aquatic environment in the area of Nea Michaniona is not ideal for the growth of aquatic life. The increased alkalinity (Fig. 4) of the water and its reducing nature, due to the presence of microorganisms and pollutants are negative factors. Also, the low salinity, combined with the relatively high temperature creates an environment that is

not beneficial to the health and growth of species, although parameters such as conductivity (Fig.5) and dissolved oxygen (Fig. 6) are within acceptable ranges.

Fig. 3 Measurements points in Nea Michaniona, Thessaloniki, Greece

Table II. Measurements of aquatic environment of Nea Michaniona

Sensor Type	Values		
	First point	Second point	Third point
pH	9.3	9.338	9.37
ORP (mV)	-23.9	-14.07	-18.28
EC (μS/cm)	5542.55	6602.76	5757.25
TDS (ppm)	2993.16	3565	3109.25
Salinity (ppt)	2.99	3.60	3.11
Specific Gravity	1.003	1.003	1.003
Temperature	27.23	27.83	27.14
DO (mg/L)	7.15	6.23	7.67
Oxygen Saturation (%)	91.06	80.34	84.37

IV. CONCLUSIONS

In this paper, a low-cost system for measuring environmental parameters of sea water environments using IoT was developed and tested under real conditions. The main contribution of the study lies in the design and implementation of a system that can measure in real time physicochemical parameters for the purpose of sea water quality assessment. The system provides the ability to measure a list of water quality parameters like pH, ORP, DO, EC etc, by means of only three probes and an appropriate communication protocol that allows such an integration. The results of testing the system in the areas of Halastra and Nea Michaniona in Thermaikos Gulf showed that it is capable of producing reliable measurements of water parameters. The ability to monitor the sensors in real time and store the measurements locally is an important advantage, as there is immediate access to the information and timely intervention if needed.

V. COPYRIGHT

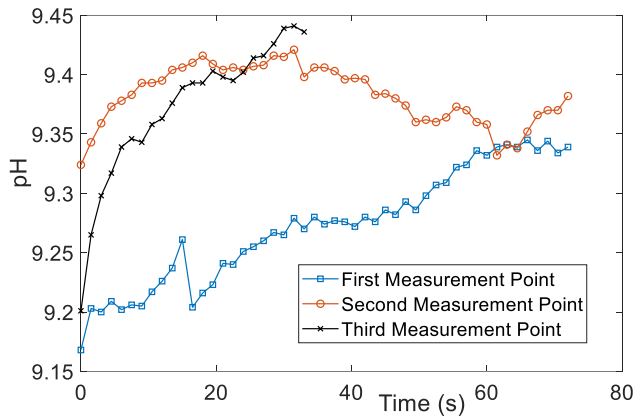materials, has been created by the authors listed in the submission email.

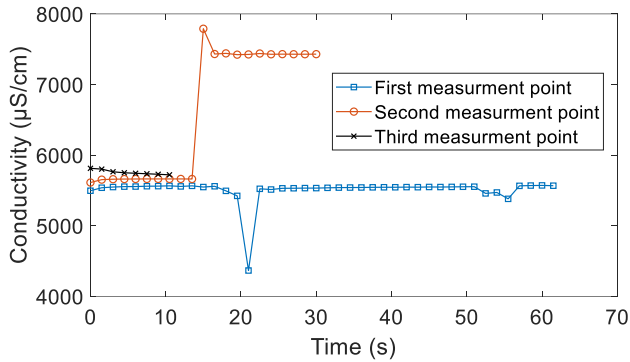**Fig. 4 Measurements of pH in Nea Michaniona**
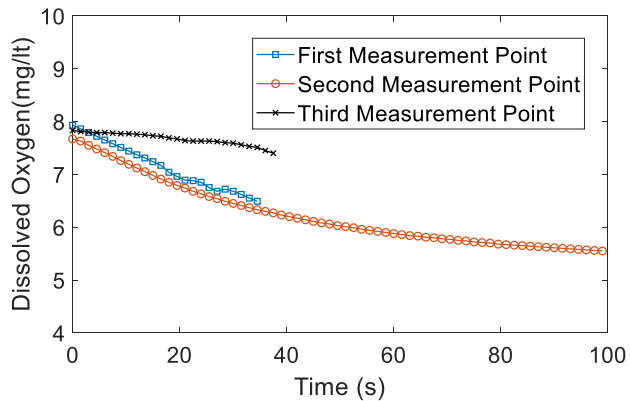

Fig. 5 Measurements of Conductivity in Nea Michaniona

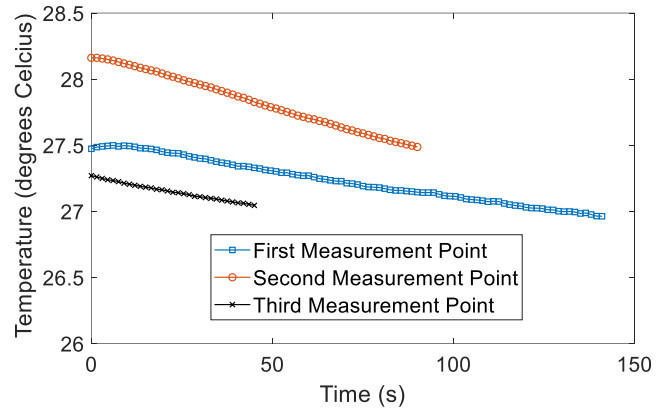**Fig. 6 Measurements of Dissolved Oxygen in Nea Michaniona**

Fig. 7 Measurements of Temperature in Nea Michaniona

REFERENCES

[1] Budiarti, R. P. N., Tjahjono, A., Hariadi, M., & Purnomo, M. H. (2019). Development of IoT for Automated Water Quality Monitoring System. Proc. ICOMITEE 2019, October 16th-17th 2019, Jember, Indonesia https://doi.org/10.1109/icomitee.2019.8920900 [2] Lakshmikantha, V., Hiriyannagowda, A., Manjunath, A., Patted, A., Basavaiah, J., & Anthony, A. A. (2021). IoT based smart water quality monitoring system. Global Transitions Proceedings, 2(2), 181–186. https://doi.org/10.1016/j.gltp.2021.08.062

[3] Chowdhury, A. a. S., Arafat, Y., & Alam, M. S. (2022). IOT-GSM based controlling and monitoring system to prevent water wastage, water leakage, and pollution in the water supply. 2022 International Conference on Innovations in Science, Engineering and Technology (ICISET). https://doi.org/10.1109/iciset54810.2022.9775876

[4] Yaroshenko, I., Kirsanov, D., Marjanovic, M., Lieberzeit, P. A., Korostynska, O., Mason, A., Frau, I., & Legin, A. (2020). Real-Time Water Quality Monitoring with Chemical Sensors. Sensors, 20(12), 3432. https://doi.org/10.3390/s20123432

[5] Vijayakumar, N., & Ramya, R. (2015). The real time monitoring of water quality in IoT environment. IEEE Sponsored 2nd International Conference on Innovations in Information,Embedded and Communication Systems (ICIIECS)2015. https://doi.org/10.1109/iciiecs.2015.7193080

[6] Khatri, P., Gupta, K. K., & Gupta, R. K. (2019). Raspberry Pi-based smart sensing platform for drinking-water quality monitoring system: a Python framework approach. Drinking Water Engineering and Science, 12(1), 31–37. https://doi.org/10.5194/dwes-12-31-2019

[7] Cloete, N. A., Malekian, R., & Nair, L. (2016b). Design of smart sensors for Real-Time Water Quality Monitoring. IEEE Access, 4, 3975–3990.https://doi.org/10.1109/access.2016.2592958

[8] Atlas Scientific. (2022). *Pi sample code*. Atlas Scientific. https://files.atlas-scientific.com/pi_sample_code.pdf

[9,10] GREECE SHELLFISH CULTIVATION IN GREECE. (n.d.).https://www.fao.org/4/S6087E/S6087E02.html

Design and construction of a data recording system for the powertrain of an electric vehicle

Amalia Kyriazopoulou, Theodoros Kosmanis [0000−0002−8730−1345] and Dimitrios Tziourtzioumis [0000−0002−1881−3953]

International Hellenic University, Alexander University Campus, 57400, Sindos, Greece

amaliakyriazopoulou@gmail.com

Abstract— **This study focuses on designing and constructing an experimental setup for recording signals from electric vehicle sensors. The developed data recording system is an automated platform enabling real-time monitoring of battery parameters based on voltage levels from a series of sensors. The supporting software was developed using the Arduino IDE, featuring both a codebase and a user-friendly interface that simplifies sensor readings and interpretation.**

Keywords— **Data Acquisition Systems, Electromobility.**

I. INTRODUCTION

The rapid growth of electromobility has created a demand for efficient and cost-effective solutions to monitor and evaluate the performance of electric vehicles (EVs). Data acquisition systems play a critical role in capturing key operational parameters, such as battery performance, motor efficiency, and sensor outputs. However, traditional data acquisition systems are often expensive and complex, making them less accessible for research, prototyping, and educational purposes [1]. To address this gap, low-cost data acquisition systems offer a viable alternative, providing real-time monitoring capabilities while maintaining simplicity and affordability. These systems enable researchers and developers to analyze crucial data, optimize EV performance, and support advancements in sustainable transportation technologies [2].

Low-cost data acquisition systems are particularly advantageous in fostering innovation within the electromobility sector. By leveraging affordable hardware components, such as microcontrollers and open-source platforms, these systems can be tailored to specific applications without sacrificing functionality. They are ideal for small-scale research projects, academic experiments, and startups aiming to develop and test EV technologies on limited budgets. Furthermore, the integration of real-time data processing and user-friendly software interfaces enhances their accessibility, allowing users to efficiently monitor parameters like voltage, current, temperature, and state-of-charge [3]. These attributes make low-cost systems an essential tool for driving progress in electric vehicle design, energy management, and sustainability efforts.

The data acquisition system proposed in this study enables real-time monitoring of battery parameters using voltage levels from a series of sensors. The setup incorporates three key sensors: a current transducer, a voltage transducer, and a temperature sensor. Each sensor provides essential information about the energy storage system of the vehicle. Continuous monitoring of these parameters is crucial for achieving optimal functionality and efficiency of the battery.

The data acquisition platform is built around the Arduino Uno microcontroller. The custom Arduino IDE [4] code developed for this platform facilitates the collection and storage of data received as signal voltages. Additionally, the code processes the data to generate useful insights into the battery's health condition. The resulting information is presented in a user-friendly interface for easy interpretation.

The experimental setup serves as a flexible platform for studying energy storage systems, enabling easy control and analysis of individual sensors. This data acquisition application enhances the understanding of the functionality and potential malfunctions in the energy storage systems of electric vehicles. Furthermore, it contributes significantly to both educational and research efforts in the field of electromobility.

II. DATA RECORDING PLATFORM

Within the scope of this article, a comprehensive study was conducted, along with the design and construction of a system to measure voltage, current, and temperature from the powertrain of an electric vehicle. The system developed as part of this research includes the following components: Electric vehicle, Temperature sensor, Current transducer, Voltage transducer, Microcontroller and Thermocouple amplifier.

The electric vehicle used for this study was the EcoCar City, a compact urban passenger car powered by rechargeable battery arrays and a 7.5 kW AC electric motor. Its straightforward design made it an ideal choice for the study's requirements. The vehicle is equipped with six deep-cycle lead-acid batteries, each rated at 12.5V, connected in series to deliver a total system voltage of 72V.

In the preliminary stage, determining the range of parameters under investigation was crucial for developing a reliable data acquisition system. While the electric vehicle's voltage was known to be approximately 72 V, the powertrain's current-unspecified by the manufacturer-remained unknown. The primary goal was to identify the maximum current the vehicle could achieve under operational conditions.

To achieve this, the vehicle was securely positioned on the Cartec LPS2510 chassis dynamometer, as shown in Fig.1, located in the Department of Industrial Engineering and Management at the International Hellenic University. Its rear wheels were placed on the rollers, as the vehicle features rear-wheel drive. A precise and reliable measurement system was essential for the procedure. For this purpose, a Tektronix TBS 1000C series oscilloscope was used. Necessary modifications were made to the oscilloscope's probe connections, and all wiring was thoroughly insulated. The power supply was disconnected to ensure the safe connection of the probes to the vehicle's inverter.

Once the setup was complete, the vehicle's power system was activated, and the throttle position was gradually increased using the accelerator. Tests were conducted under load conditions applied by the dynamometer and during simulated braking scenarios. The peak current recorded during the experimental procedure was 150 A.

Fig. 1. Electric vehicle secured on chassis dynamometer.

Based on the previously obtained measurements, sensors were selected to monitor the voltage, current, and temperature of the vehicle's powertrain.

Initially, it was essential to select the appropriate sensors, followed by the construction of a test bench setup. This setup was necessary to test the sensor connections and verify that the selected sensors met the project's requirements. Once it was confirmed that the setup was functioning correctly, it was transferred to the vehicle, ensuring that all necessary safety precautions for working with high-voltage systems were followed.

The microcontroller selected for this project was the Arduino Uno, which proved to be an ideal choice for the initial phase of the thesis. Its user-friendly design, both in terms of hardware

and programming, made it particularly well-suited for this application. The simplicity of its design and ease of integration with various components facilitated efficient experimentation and testing during the early stages of the project.
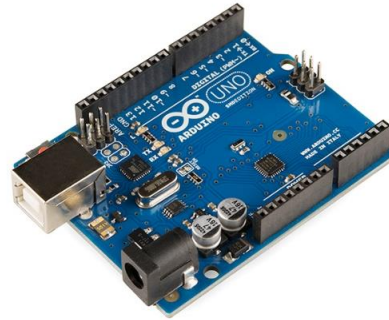

Fig. 2. Microcontroller Arduino Uno.

A. Current transducer: LEM HASS-100S [5]

Specifically, the HASS 100S sensor from LEM was selected for its ability to measure currents up to 300 Amperes. The HASS-50 sensor, with a maximum current of 150 Amperes, was not chosen because maintaining a safety margin was deemed essential for ensuring more accurate measurements.

Fig. 3. LEM Hass-100s current transducer. [5]

To establish the necessary connections on the Arduino, a breadboard, wires, and resistors were used. First, the 5V pin of the Arduino was connected to the breadboard's positive rail, and the GND pin was connected to the negative rail. The negative rail was then linked to the sensor's ground pin (detail 1, 3). Next, the Arduino's analog input A1 was connected to a resistor and subsequently to the sensor's output (detail 1, 2). Finally, the analog input A2 of the Arduino was connected to the U_{ref} pin of the sensor (detail 1, 1).
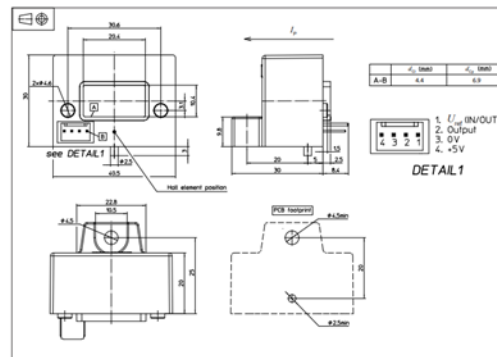

Fig. 4. Technical drawing of Hass-100S. [5]

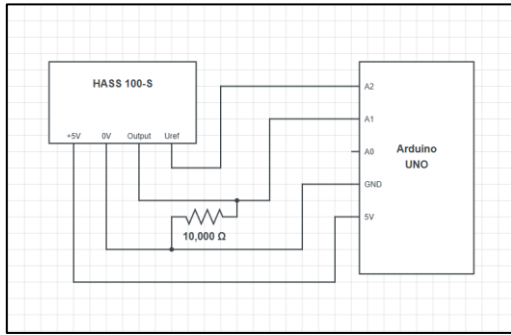The diagram below illustrates the connection of the sensor to the microcontroller.

Fig. 5. Connection diagram of Hass-100S.

Subsequently, the Arduino was programmed to implement the required functionality.

B. Voltage transducer: LEM DVL 125 [6]

For monitoring the battery voltage, the DVL125 voltage transducer from LEM was selected. This transducer can handle voltages up to 125V, exceeding the battery voltage of 72V, and is designed to convert high voltages into a lower-range current suitable for processing by the microcontroller. The sensor's connection starts with its power supply: the ±Uc terminals are connected to a ±15V voltage source, as specified in the datasheet (Appendix 2). The ±HV terminals are then connected to the positive and negative terminals of the battery being monitored. The ground of the voltage transducer is connected to a 50.5 Ω resistor, with the other end of the resistor linked to the Arduino's ground. Finally, the Arduino's analog input A0 is connected to the first terminal of the resistor. A breadboard was used to ensure safe and reliable connections throughout the setup.

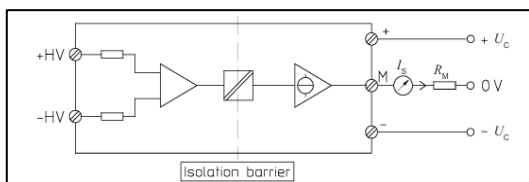Fig. 6. Voltage transducer LEM DVL 125. [6]

Fig. 7. Connection diagram of LEM DVL125.

C. Temperature sensor [7]

Next, the temperature sensor was tested using a Type K thermocouple paired with a thermocouple amplifier. The

MAX31856 amplifier from Adafruit was selected for this purpose, as shown in the accompanying image.
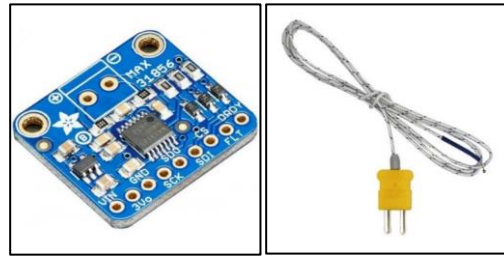

Fig. 8. MAX31856 thermocouple amplifier (left) and Type K thermocouple (right). [7]

The wiring process began with soldering a 2-pin terminal block to connect the thermocouple and a pin header for interfacing with the amplifier. The Vin pin of the amplifier was connected to the positive rail of the breadboard, which in turn was connected to the 5V pin of the Arduino. The GND pin of the Arduino was connected to the negative rail of the breadboard, and the negative rail was linked to the GND pin of the amplifier. Next, the SCK, SDO, SDI, and CS pins of the amplifier were connected to the Arduino's Digital pins 13, 12, 11, and 10, respectively. The connection between the sensor and the microcontroller is illustrated in the diagram below:
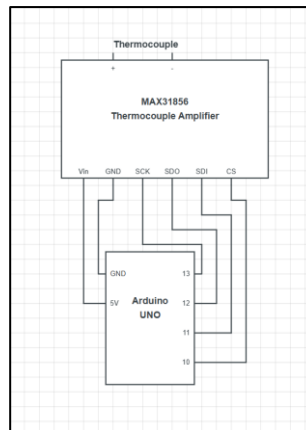

Fig. 9. Connection diagram of Thermocouple Amplifier.

After verifying the proper functioning of all sensors on the test bench using tools such as a thermometer, ammeter, and multimeter, the system was ready to be transferred from the bench to the vehicle.
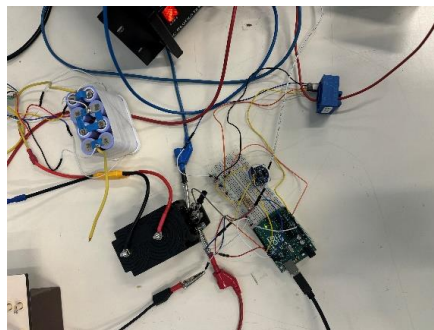
D. Benchmarking tests and results

Fig. 10. Test bench setup.

Since the system would be taking measurements while the vehicle was in motion, ensuring maximum stability was essential. To achieve this, the breadboard was replaced with connectors, providing a more secure and stable connection. The current sensor was safely mounted on the positive terminal of the vehicle's inverter, while the voltage sensor was connected to the vehicle's battery and powered by the same source. The thermocouple was placed in the area where the vehicle's batteries were stored. Once the wiring was properly completed, the Arduino was connected to a laptop via an USB cable. The code was uploaded, and the first measurements from the vehicle appeared, confirming that the system was fully operational.

The vehicle was then moved to the dynamometer, and the first measurements were taken. Initially, a test was conducted without applying any load from the dynamometer, gradually increasing the vehicle's speed until it reached 70 km/h. Following this, tests were performed with a 600 kg load, and then with a load of one ton.

Below is the graph illustrating the voltage and current measurements during the test conducted with a one-ton load. It can be observed that as the discharging current (blue line) increases, the battery voltage (orange line) decreases, and vice versa. The temperature changes were negligible and, therefore, have been omitted from the graph.
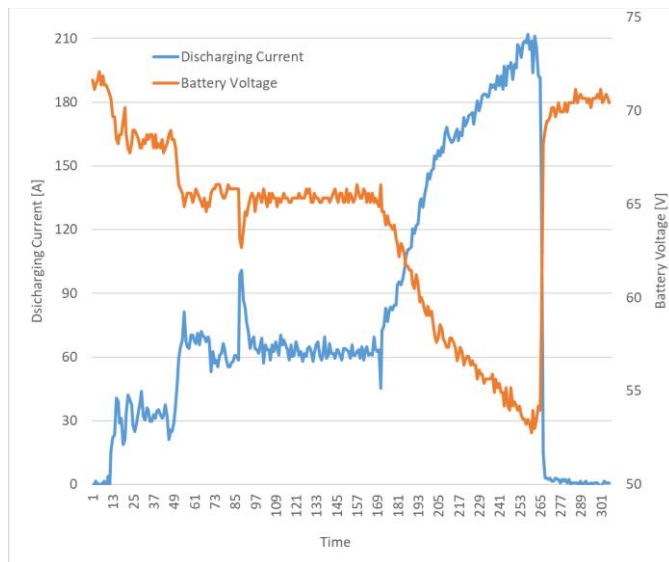

Fig. 11. Distribution of battery voltage and discharging current under varying braking forces applied to the wheels by the chassis dynamometer.

The vehicle was then moved outside the laboratory to test the measurement system under real-world urban conditions. The test route included various driving scenarios, such as gradual acceleration, complete stops, starts from a stationary position, altitude variations (e.g., potholes and speed bumps), and changes in road surface profiles. These measurements were taken using the vehicle's eco mode, with the headlights and other auxiliary systems turned off to minimize additional power consumption. Below is the graph illustrating the voltage and current measurements during the test under real-world conditions.
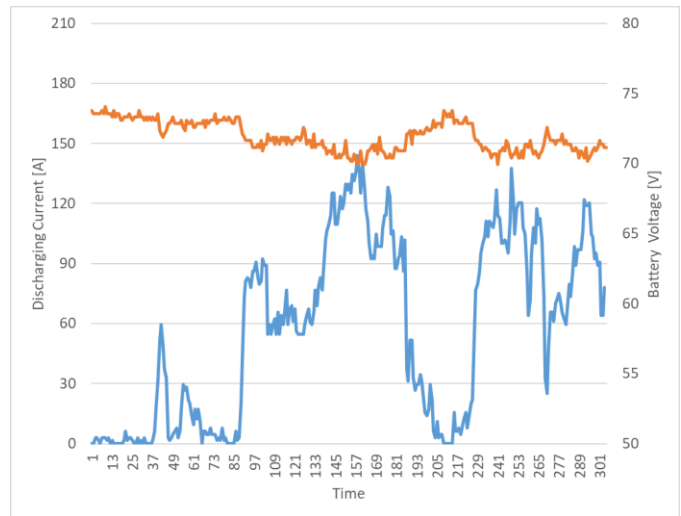

Fig. 12. Distribution of battery voltage and discharging current under real driving conditions.

III. CONCLUSIONS

Through the development and use of code in the Arduino IDE, efficient monitoring of energy storage system parameters, such as voltage and discharging current, was achieved. The ability to measure these parameters in real-time provides significant advantages in understanding battery operation.

The data acquisition platform developed in this study proved to be both functional and efficient in collecting reliable data, making it a valuable tool for future research and testing in energy storage systems. Its flexibility allows adaptation to different types of sensors or other applications where parameter analysis is needed. This makes it ideal for both research and educational use in laboratory environments.

IV. COPYRIGHT

All content included in this submission, including but not limited to text, figures, tables, and supplementary materials, has been created by the authors listed in the submission email.

REFERENCES

[1]   J. Beretta, *Automotive Electricity – Electric Drives*: ISTE Ltd and John Wiley & Sons, Inc, 2010.

[2]   J. G. Hayes and G. A. Goodarzi, *Electric Powertrain – Energy Systems, Power Electronics and Drives for Hybrid, Electric and Fuel Cell Vehicles*: John Wiley & Sons Ltd, 2018.

[3]   C. D. Rahn and C. Y. Wang, *Battery Systems Engineering*: Wiley and Sons, 2013.

[4]   Arduino, "Arduino Uno R3 - Product Reference Manual," 2024.

[5]   LEM, "Current Transducer HAS 100-S/SP105 - Technical Datasheet," 2024.

[6]   LEM, "Voltage transducer DVL 125 - Technical Datasheet," 2024.

[7]   Adafruit, "Adafruit MAX31856 Universal Thermocouple Amplifier - Technical Datasheet," 2024.

Design and construction of a data acquisition device for a gasoline internal combustion engine management system

Evangelia Meimaroglou, Dimitrios Tziourtzioumis[0000−0002−1881−3953], and
Theodoros Kosmanis[0000−0002−8730−1345]

International Hellenic University, Alexander University Campus, 57400, Sindos, Greece

evelinameimaroglou@gmail.com

Abstract— **This study focuses on the development (design and construction) of an experimental setup for data acquisition and processing of signals from sensors of a gasoline engine management system. The developed data acquisition is an automated platform that enables real-time monitoring and analysis of critical automotive engine parameters, based on the voltage levels of a series of sensors. The software tool to support the data acquisition hardware was developed on the LabVIEW® software as a code as well as a foreground environment that makes sensor reading and understanding particularly straightforward.**

Keywords— **Data Acquisition Systems, Automotive Engine management, Automotive Electronics.**

I. INTRODUCTION

AUTOMOTIVE Engine Control Units (ECUs) are becoming extremely complicated with time. From purely mechanical decades ago, they have evolved to fully automated nowadays [1]. The race to decrease the exhaust gases and to increase fuel economy by maintaining at the same time a balanced performance has led to the need of controlling almost every process in the internal combustion engine. Automotive engine electronics have also become complicated. As the number of sensors and actuators increases, the requirement for integration of various parts in order to reduce response time becomes more imperative [2].

The aforementioned evolution is also apparent in the automotive educational sector which must follow. However, although engine management and automotive electronics technology evolves, students and apprentices in general must be able to understand and learn starting from the very basics and proceed to more advanced knowledge. In this context, the need for equipment that will provide reliable engine components monitoring and at the same time insight to operation fundamentals is apparent. Every higher education lab in the automotive electronics sector requires specialized to adequately train students.

The data acquisition platform proposed in this study enables real-time monitoring and analysis of critical automotive engine parameters, based on the voltage levels of a series of sensors.

The setup focuses on four primary automotive engine sensors: the inductive speed sensor, the coolant temperature sensor, the throttle position sensor, and the pressure sensor. Each sensor provides essential information for engine performance. Continuous monitoring of these parameters is crucial for achieving optimal functionality and efficiency of the automotive internal combustion engine. The data acquisition platform is based on the NI DAQ hardware series (chassis and data acquisition cards). The LabVIEW® code that was developed allows the collection and storage of data received as signal voltages. The code also enables data processing in order to allow useful insights about the engine condition. The information produced is depicted on a corresponding user friendly environment. The quality of the developed hardware and software system is validated by corresponding results received by an automotive educational unit.

The experimental setup that was developed is a flexible platform for studying and testing various engine management systems, allowing for easy control and analysis of individual sensors. The ability to understand the functions and possible malfunctions of the automotive internal combustion engine is enhanced through this data acquisition application, contributing to both educational and research in automotive systems.

II. DATA ACQUISITION PLATFORM

An ignition system simulation board, for educational purposes (Fig. 1), was the main measurement unit used in order to test the developed data acquisition system. It includes basic components of an automotive ignition system, such as: double ignition coils, spark plugs, throttle body incorporating the corresponding position sensor, engine coolant temperature sensor, mass absolute pressure (MAP) sensor, engine control unit, vehicle speed sensor, injectors and fuel pump. An additional board, simulating engine management system circuit was the means to connect the external data acquisition platform to its sensors and other components (Fig. 1).

The basic component of the data acquisition platform was the chassis NI cDAQ-9174 (Fig. 2), which equipped with NI 9219 (Fig. 3) and NI 9201 (Fig., 4) cards can perform high quality and accuracy measurements. The values to be acquired by the

platform were from the throttle position sensor, the coolant temperature sensor and the manifold absolute pressure sensor, the voltage signals of which are characterized by relatively small time variations (tens of Hz), and from the speed sensor, which provides high speed sinusoidal signals (a few thousands of Hz). In the subsections to follow, the measuring equipment is more detail.
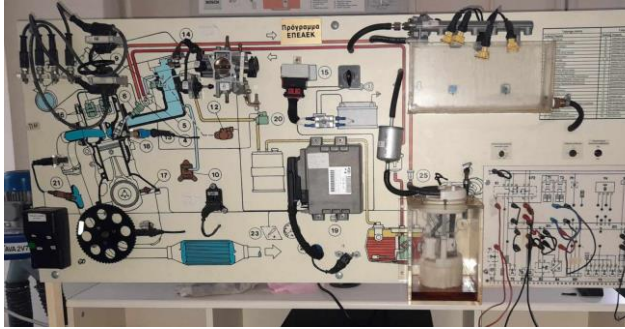

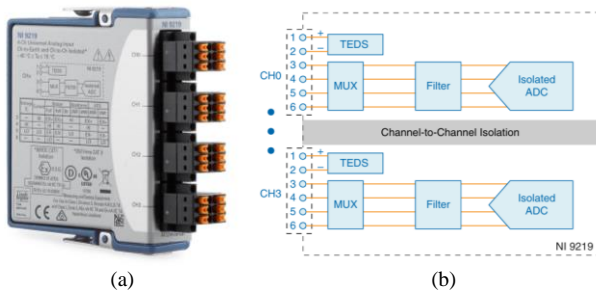Fig.1. Ignition system board and its circuit

Fig. 2. NI cDAQ 9174 chassis. [3]

(a)   (b)
Fig. 3. (a) NI 9219 card and (b) Block diagram of the internal circuit. [4]

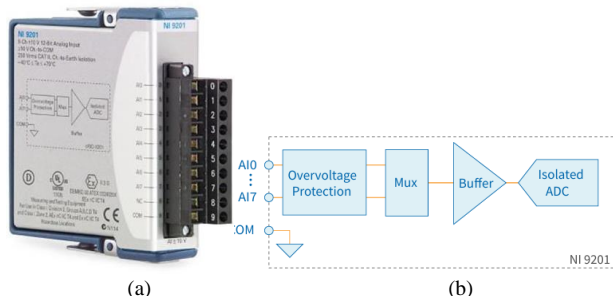(a)   (b)
Fig. 4. (a) NI 9201 card and (b) Block diagram of the internal circuit. [5]

A. NI cDAQ 9174 chassis [3]

The chassis NI cDAQ 9174 provides the plug-and-play simplicity of USB to sensor connections and electrical measurements. It also controls the timing, synchronization, and data transfer between C Series I/O modules and an external host. It can be used with a combination of C-Series I/O modules to create a combination of analog I/O, digital I/O, and counter/timer measurements. The cDAQ-9174 also features four 32-bit general-purpose counter/timers (Fig.2).

B. NI 9219 card [4]

The NI 9219 card is a universal C-Series module designed for multi-purpose testing on any NI CompactDAQ or CompactRIO chassis. The NI 9219 card is an analog signal card that enables measurement of multiple signals from sensors, such as strain gauges, RTDs, thermocouples, load cells, and other powered sensors. Its four channels are individually selectable, allowing you to perform a different type of measurement on each channel. The measurement ranges vary for each measurement type and include up to ±60V for voltage and ±25mA for current. (Fig.3)

The NI 9219 card can measure in a temperature range of -40 degrees Celsius to +70 degrees Celsius. The maximum sampling rate is 100 samples per second per channel, with the difference that the sampling rate for thermocouples is 50 samples per second per channel.

This card is applied to measurements for the throttle position sensor, pressure sensor and temperature sensor.

Input characteristics:
- Number of channels: 4 analog input channels
- ADC resolution: 24 bits
- ADC type: Delta-sigma (with analog pre-filtering)
- Sampling mode: Simultaneous

C. NI 9201 card [5]

The NI 9201 card is an analog input module for CompactDAQ and CompactRIO systems. The NI 9201 provides eight ±10 V input channels with a sampling rate of 500 kS/s. The NI 9201 card has the ability to measure in a temperature range of -40 degrees Celsius to +70 degrees Celsius. This card is applied to the measurements for the speed sensor, because a high sampling rate is necessary for valid results. (Fig. 5)

Input characteristics:
- Number of channels: 8
- ADC resolution: 12 bits
- ADC type: Successive approximation register (SAR)

III. MEASUREMENTS AND RESULTS

The equipment described in the previous section was utilized in order to perform measurements to the automotive engine management unit of Fig. 1. The data acquisition platform was composed of the hardware unit and the supporting software. The measurements were performed for four sensors. For the three sensors with low sampling rate requirement, the NI 9219 card was used whereas for the speed sensor, NI 9201 card was found more appropriate. Connections between the sensors and

the NI cards were easy due to the existence of the engine management circuit board.

The supporting control program was implemented in the LabVIEW® software which was fully compliant with the NI equipment. A virtual instrumentation board was developed for each sensor in order to allow straightforward reading of the measured values whereas all data acquired were stored in corresponding files. An analysis of the measured values per sensor and the virtual instrumentation boards is made in the below.

A. Throttle Position Sensor

The full Front Panel of the virtual board for data acquisition from the throttle position sensor is depicted in Fig. 5. The throttle position sensor's voltage graph, voltage values such as ground, supply voltage and signal voltage, as well as an angle indicator meter are shown. The sensor voltage versus time graph of Fig. 5 presents some indicative cases that are found in automotive throttle position sensors and certainly are subject of discussion in automotive electronics courses.

In case "1", signal voltage is measured as zero and corresponds to a faulty power supply connection. Similarly, case "2" indicates that there is a faulty grounding of the sensor and therefore the return voltage equals to that of the power supply, i.e. 6V. Both cases correspond to an automatic diagnosis procedure performed by the electronic control unit. In case "3", the throttle valve was gradually opening and closing, so it is observed that the voltage gradually increases and decreases, but it never reaches the minimum and maximum values of zero and six, respectively, as expected. In case "4", the throttle valve opens and closes abruptly. Therefore, the measured voltage changes steeply with time, either increasing or decreasing according to the movement of the throttle pedal

and valve, again as expected. It is observed that the response of the system is satisfying in all cases.

B. Engine Speed Sensor

The case of the engine speed sensor is somehow more difficult than that of the other sensors due to the fact that the speed is measured inductively based on the teeth of the crankshaft flywheel. The speeds achieved may reach 8000rpm, which means that the sampling frequency must exceed 16kHz. That is why the NI 9201 card is used. The sinusoidal waveform of the voltage sensor is reconstructed with accuracy as depicted in Fig. 6. In this measurement, voltage waveform frequency is measured at 2.8 kHz, which corresponds to 2800 rpm for a 60 teeth flywheel.

C. Engine Coolant Temperature Sensor

In the figure 9, it is indicated the engine coolant temperature sensor's voltage graph and resistance graph.

In the first case, sensor measured environment temperature. In the second case, sensor measured low temperature, so voltage value started to increase. In the third case, sensor measured lukewarm temperature and voltage value started to decrease. In the fourth case, sensor measured hot temperature and voltage value decreased further.

D. Manifold Absolute Pressure Sensor

In the figure 10, it is indicated the manifold absolute pressure sensor's voltage graph.

In the first case, at the start of the measurement the sensor measured atmospheric pressure and the voltage was at 4.5 Volts. In the second case, the voltage is set to zero, because it is applied under pressure equal to -1 bar with the vacuum pump. In the third case, the under pressure is gradually increased.
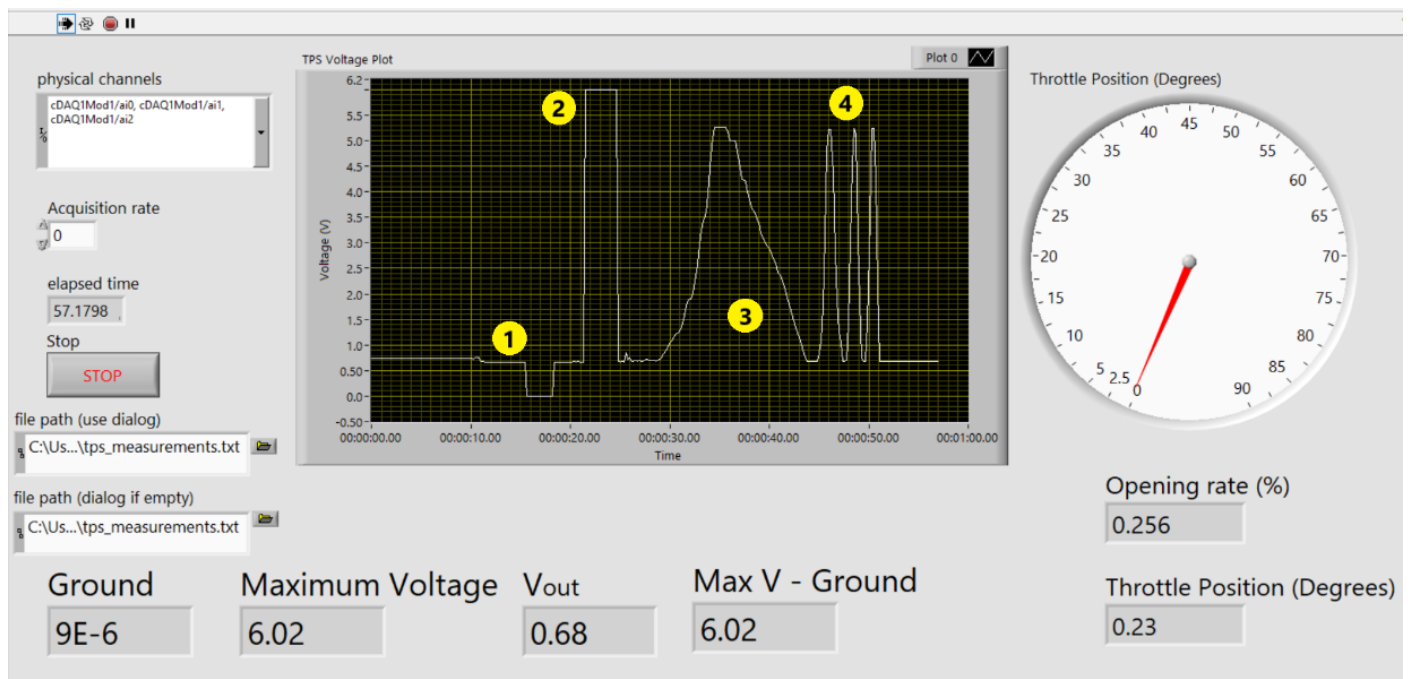

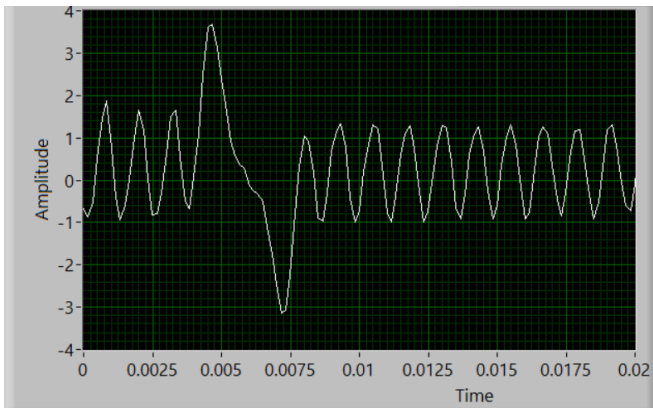Fig. 5. Throttle Position Sensor measurements virtual panel.

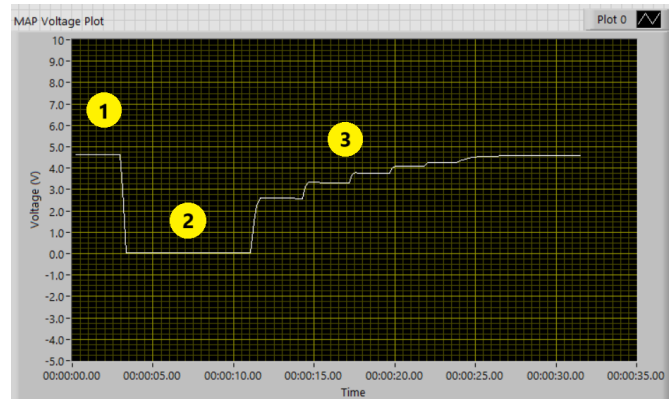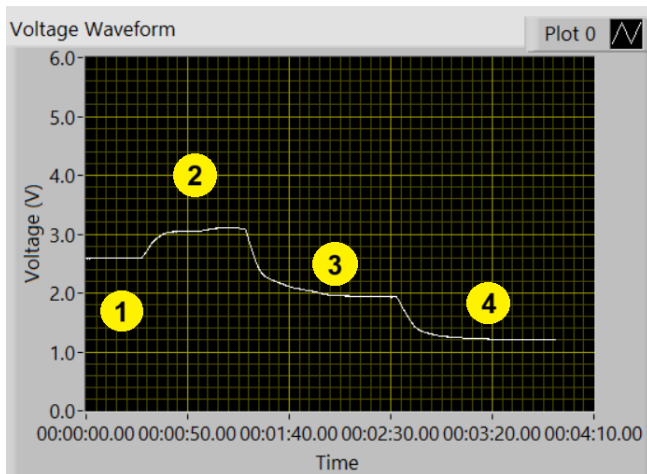Fig. 6. Vehicle speed sensor's voltage signal.

Fig. 7. Engine Coolant Temperature sensor's voltage signal.

IV. CONCLUSIONS

Through the development and utility of code in LabVIEW® software, efficient monitoring of critical automotive engine parameters, such as voltage, temperature, speed and manifold pressure, was achieved. The ability to measure these parameters in real time offers significant advantages in understanding engine operation and detecting potential malfunctions.

Fig. 8. Manifold Absolute Pressure sensor's voltage signal.

The data acquisition platform developed in this paper, proved to be functional and efficient in collecting reliable data, which makes it a useful tool for future studies and tests in engine management systems. Its flexibility allows it to be adapted to different types of sensors or even to other applications where analysis of such parameters is required. This makes it ideal for research purposes as well as for educational use in laboratory environments.

V. COPYRIGHT

All content included in this submission, including but not limited to text, figures, tables, and supplementary materials, has been created by the authors listed in the submission email.

REFERENCES

[1] T. Denton, Automobile Electrical and Electronic Systems, 3rd ed., Elsevier Butterwoth-Heinemann, 2004 (ISBN: 0-7680-1497-2).

[2] R. Bosch GmbH, Automotive Electrics – Automotive Electronics (5th edition), J. Wiley and Sons Ltd., West Sussex, 2007 (ISBN: 978-0-470-51937-0).

[3] "NI cDAQ 9174 specifications," Available: https://www.ni.com/docs/en-US/bundle/ni-9219-specs/page/specs.html, last accessed on 19/10/2024.

[4] "NI 9219 specifications," Available: https://www.ni.com/docs/en-US/bundle/cdaq-9174-specs/page/specs.html, last accessed on 19/10/2024.

[5] "NI 9201 specifications," Available: https://www.ni.com/docs/en-US/bundle/ni-9201-specs/page/specs.html, last accessed on 19/10/2024.

Study, calibration and experimental operation of sonar for surveying sea or lake bottom

Konstantina-Maria Soulaki, Dimitrios Tziourtzioumis [0000−0002−1881−3953] and
Theodoros Kosmanis [0000−0002−8730−1345]

International Hellenic University, Alexander University Campus, 57400, Sindos, Greece

kmsoulaki@gmail.com

Abstract—**This article examines the calibration and experimental operation of a sonar scanning system for surveying the seabed. It focuses on sonar systems, categorized into active and passive types. Active systems emit sound waves and use their echoes to determine the distance and orientation of objects, while passive systems detect environmental sounds. The main types of echobolistics are analyzed, emphasizing their applications in bathymetry and seabed mapping. Additionally, the paper explores the use of sonar in remotely operated underwater vehicles (ROUVs) for mapping missions. The experimental setup included the Deeper Pro+ for bathymetry and the Chasing F1 for sonar navigation. Four tests were conducted at two locations: Nea Michaniona and fishermen's huts in Chalastra. These tests produced maps depicting seabed topography and depth. Sonar data were saved as csv files, and maps were created from these records. Using Google Maps, the scanned areas were overlaid onto real-world maps. In conclusion, the article evaluates the accuracy and effectiveness of sonar systems under real-world conditions. The Deeper Pro+ proved to be a reliable tool for quick measurements at varying depths, although its accuracy depended on water conditions and proper equipment setup.**

Keywords—**Sonar USV Bathymetry Seabed Mapping**

I. INTRODUCTION

This article focuses on the study, calibration, and experimental operation of a sonar scanning and mapping system for the seabed in aquatic environments under real operational conditions. Specifically, it presents bathymetric maps of two areas near the city of Thessaloniki, created using single-beam sonars and unmanned remotely controlled surface vehicles developed by the Research Group "Hippalus" at the International Hellenic University. Field measurements were conducted between April and July 2024.

The study aims to evaluate the accuracy and effectiveness of sonar systems for mapping applications, analyse the challenges encountered under varying water conditions, and provide recommendations for improving their use. The results indicate that the Deeper Pro+ delivers reliable measurements across different depths, though its accuracy is influenced by water conditions and proper equipment setup.

II. MEASURING EQUIPMENT

The experimental equipment consists of a single-beam echo sounder (Deeper Pro+) and the Chasing F1 unmanned surface vehicle (USV).

Fig. 1. Experimental equipment.

A. Deeper Pro+

Sonar operates by sweeping in cone-shaped patterns rather than straight lines. The readings represent data collected from a broader area beneath the sonar. Notably, the area covered by the sonar widens as the scanning depth increases due to the conical nature of the scans.[1]

Wide-beam scanning, typically with an angle of 40° to 60°, is ideal for quickly surveying large areas and obtaining general information about depth and bottom structure. However, this method sacrifices accuracy and detail. It is particularly effective in shallow water, as the wider cone covers a larger area at greater depths [2]. In contrast, narrow-beam scanning, with an angle of about 10° to 20°, provides more detailed and precise imagery but covers a smaller area. This type of scanning is better suited for identifying the exact location of objects and is more effective in deeper water, where the cone's spread is limited [3]. The Deeper Pro+ used in these measurements offers two adjustable cone angles: a wide beam of 55° and a narrow beam of 15°.[4]
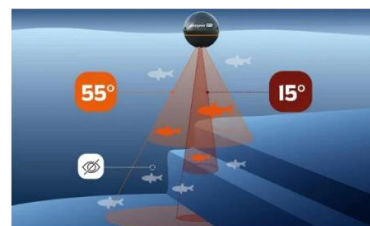

Fig. 2. Visible and non-visible scanning area.[4]

Another factor to consider regarding the width of the sonar cone is the "blind zone," an area directly beneath the surface of the water where objects may not be detected. The size of this blind zone decreases with higher sonar frequencies. However, any object located within the blind zone will not appear in the sonar image.[5, 6]

Before conducting tests in real aquatic environments, it is essential to perform experiments under controlled laboratory conditions [7]. Initial tests were conducted in a tank at the Energy Systems Laboratory of the Department of Production and Management Engineering at the International Hellenic University. Specifically, these tests involved using a glass of water and a tank.

During the tests, the sonar emitted a piercing sound, which is normal and not a cause for concern. However, accurate information could not be obtained at such shallow depths.

The Deeper Pro+ is accompanied by the Fish Deeper app, which can be easily downloaded onto a mobile phone via the Play Store. At the top of the app interface is the "Status Bar," which displays essential information about the sonar's status.
These include:
• Time
• Mobile battery
• Sonar battery
• Water temperature
• Speed of movement
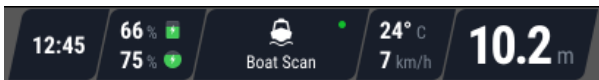• Current depth and
• Status of sonar

Fig. 3. Scanning system operating status information (device and sonar).

B. *Unmanned Surface Vehicle, Chasing F1*

This vehicle is part of the unmanned vehicle fleet of the "Hippalus" Research Group at the International Hellenic University. Specifically, the team operates five unmanned underwater remotely controlled vehicles and two unmanned remotely controlled surface vehicles. The vehicle consists of a boat equipped with four thrusters, a Li-ion 4800 mAh battery, two antennas, an underwater camera (1080P Full HD Camera Plus IR), an integrated remote-controlled spool with a 20-meter cable, a 3B Chasing remote control, and an underwater rotating camera (360°).[8]

The application compatible with the Chasing F1 is Chasing GO2, which can be easily downloaded onto a mobile phone via the Play Store.

Fig. 4. Individual parts of the surface vehicle.

Proper vehicle calibration consists of four simple steps. The first step is to position the vehicle in front of the operator with the upper part facing them. The second step is to slowly rotate the vehicle in space. The third step is to ensure the vehicle is positioned to look straight ahead. The fourth and final step is another slow rotation of the vehicle in space.

III. MEASUREMENTS

A total of four sound scans were conducted-two at the port of Nea Michaniona and two at the fishermen's huts in Chalastra. Each of the four scans will be described separately below.

A. *First sounding scan at the port of Nea Michaniona*

On April 11, 2024, the first excursion took place at the port of Nea Michaniona, Thessaloniki, to map the area. The experimental procedure lasted approximately three hours (11:30–14:30). This excursion was conducted in collaboration with Professors Mr. Tziourtzioumis, Mr. Kosmanis, and Mr. Minos, as well as student Afroditi Antoniadou. The assistance of Mr. Theofanis Karydas was also invaluable, as he transported us to the measurement point in his fishing boat.

The entire experimental process took place aboard a fishing boat in the sea. After successfully boarding the boat and reaching the desired location, the assembly of the vehicles and the installation of single-beam sonars began. Once the final checks were completed, the vehicles were lowered into the water. As previously mentioned, the sonar acquires the ability to connect wirelessly when submerged. After successfully connecting the phone to the sonar and detecting a strong GPS signal, the scan commenced. Continuous monitoring of the vehicle's connection to the sonar and the mobile phone is required throughout the process.

To better evaluate the scan results, the .csv file exported by the application was used. The record includes measurements of latitude, longitude, depth, and water temperature.

The following table shows sample measurements from the scan file.

Table 1. Presentation of the measurements of the scan file of the 1st excursion.

Latitude	Longitude	Depth (m)	Temperature (ºC)
40.46492667	22.85217167	3.75	21
		3.72	21
		3.72	21
40.464925	22.852175	3.72	21

The sea temperature during the measurements ranged from 20°C to 22°C, with no significant variation. After scanning a fairly satisfactory portion of the port, the equipment was cleaned, and the measurement processing began. It is worth noting that the sonar control application can display the scanned area on the map, as shown in the image below.
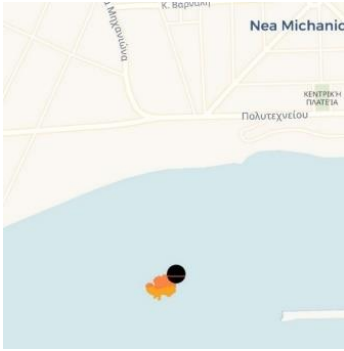
Fig. 5. Illustration of the scanning area of the port of Nea Michaniona on a geographical map.

After moving to the Energy Systems Laboratory at the Department of Production Engineering and Management of the International Hellenic University, the first-level processing of the archive began to determine whether the measurements were successfully recorded. The figure below shows the final map of the port of Nea Michaniona, combining all the individual files.
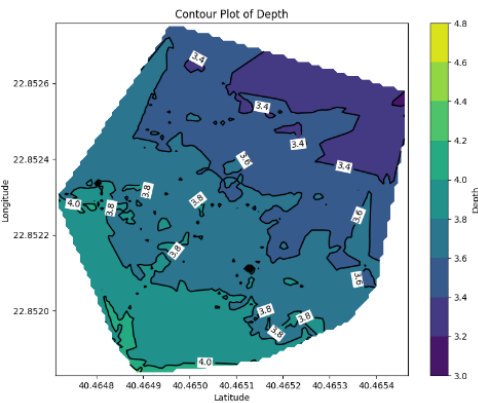

Fig. 6. Final bathymetric map of the port of Nea Michaniona.

As shown below, using the developed application, it is possible to create a .csv file containing the four (4) corner points, based on latitude and longitude, of the scan area.

Table 2. The four (4) corner points are derived from the .csv file generated by the program.

Latitude	Longitude
40.46471167	22.852295
40.46546833	22.85257333
40.464895	22.85183
40.46496333	22.85275833

Using these values and with the help of Google My Maps, the scan area is accurately depicted on the map, as shown in the image below. Additional points have been included to better visualize the scan area. Orange represents the starting point of the scan, red symbolizes the point with the maximum depth, and green indicates the point with the minimum depth.

The maximum depth was approximately 4 meters, while the minimum was 3.2 meters. The total area covered was 3.86 acres.
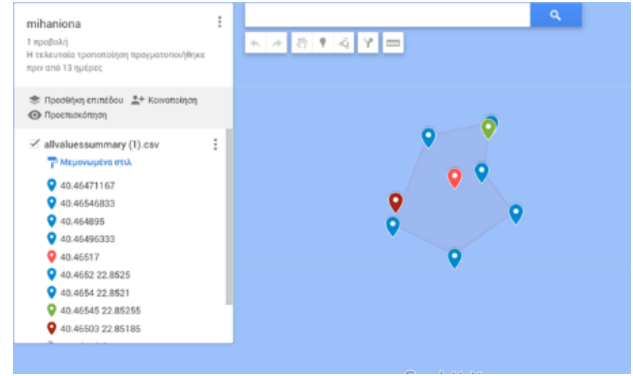

Fig. 7. Image from the map as created in Google Maps from the data of the first excursion to Nea Michaniona.

By combining all the above tools, a fairly accurate "picture" of the scanned and mapped area is obtained, as it provides combined information about both the depth and the exact location on the map where the measurements were taken.

B. Second sounding scan at the Fishermen's Huts in Chalastra

On June 6, 2024, the second excursion took place at the Fishermen's Huts in Chalastra, Thessaloniki, with the aim of mapping another area. The experimental procedure lasted about an hour (12:50-13:50). This time, the entire experimental process was conducted on land. The procedure followed was the same as the previous excursion, with the "Onshore" mode selected. However, some issues arose due to the shallow depth of the area, which was less than 0.5 meters. As a result, the sonar failed to provide accurate readings. The waves submerged the sonar, causing a loss of connection and incorrect values. Additionally, the waves made it difficult for the vehicle to navigate. The following tables include sample measurements from the scan file.

Table 3. Presentation of scan file measurements (incorrect values).

Latitude	Longitude	Depth (m)	Temperature (ºC)
40.555225	22.74146833	5.99	30
		5.96	30
		1794.24	30
		1794.23	30

Table 4. Presentation of scan file measurements (correct values).

Latitude	Longitude	Depth (m)	Temperature (ºC)
40.55517	22.741525	0.90	29
		0.90	29
		0.90	29
		0.90	29

The first table clearly shows that the values are incorrect due to the reasons mentioned above. Afterward, correct values were obtained. The sea temperature during the measurements ranged from 29°C to 31°C. Once the scan was completed, the measurements were processed, and the

resulting scan area, as depicted by the sonar application, is presented below.
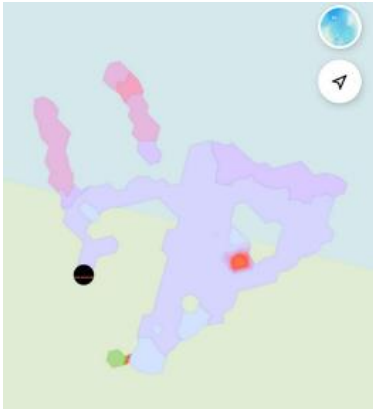

Fig. 8. Illustration of the scanning area of the fishermen's huts in Chalastra on a geographical map.

Using the application developed in Python by the Energy Systems Laboratory, the following bathymetric map was created.
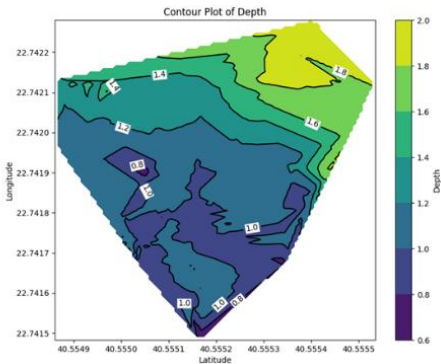

Fig. 9. Final bathymetric map of the fishermen's huts in Chalastra

Below is the generated .csv file.

Table 5. The four (4) corner points are derived from the .csv file generated by the program.

Latitude	Longitude
40.55496	22.74197167
40.555535	22.74212167
40.555225	22.74146833
40.55539833	22.74228

Using these values and with the help of Google My Maps, the scan area is accurately depicted on the map, as shown in the image below. The maximum depth was approximately 2 meters, while the minimum depth was 0.8 meters. The total area covered was 2.87 acres.
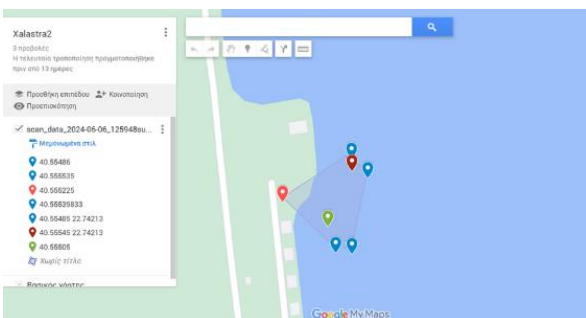

Fig. 10. Image from the map as created on Google Maps from the measurements of the second excursion to Chalastra.

As seen in the image from the sonar application and Google My Maps, it appears as though an area on land is being scanned rather than in the sea. This "error" is due to the poor updating of the maps for the area.

C. Third sounding scan at the Fishermen's Huts in Chalastra

On June 27, 2024, the third excursion took place at the Fishermen's Huts in Chalastra, Thessaloniki, with the goal of mapping another part of the area. The experimental procedure lasted about an hour (12:50-13:50). The duration of the scan was relatively short this time as well, due to unfavorable weather conditions (high temperature and sun). This excursion was carried out in collaboration with Professor Tziourtzioumis. Once again, the entire experimental process took place on land.

Similar issues arose regarding the shallow depth (>0.5m), which caused the sonar to produce incorrect values due to the wave action from the wind. Additionally, not all the scanned values were saved, resulting in a small file size with limited data. The following tables include indicative measurements from the scan file.

Table 6. Presentation of scan file measurements (incorrect values).

Latitude	Longitude	Depth (m)	Temperature (ºC)
		60.15	28
		60.02	28
		60.02	28
		60.07	28

Table 7. Presentation of scan file measurements (correct values).

Latitude	Longitude	Depth (m)	Temperature (ºC)
40.55476833	22.741615	0.93	28
		0.93	28
		0.93	28
40.55478	22.74161333	0.93	28

Looking at the initial depth values, it is clear that they are incorrect, followed by the correct values being displayed. The sea temperature remained stable at 28°C. The scan area, as shown in the sonar application, is then presented. The maximum depth measured was 0.8 meters.

Fig. 11. Illustration of the scanning area of the fishermen's huts in Chalastra on a geographical map.

It is clear that two different areas were scanned. However, due to the issues mentioned above, not enough values were saved from the first point scanned (right). Therefore, the map shown in the following image primarily depicts values from the second area scanned (left).
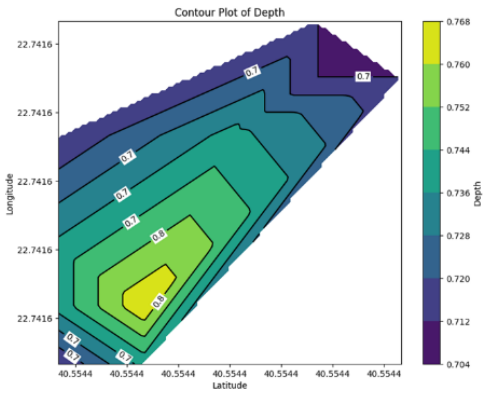
Fig. 12. Final bathymetric map of the fishermen's huts in Chalastra during the third excursion.

Below is the generated .csv file.

Table 8. The four (4) corner points are derived from the .csv file generated by the program.

Latitude	Longitude
40.554367	22.74161
40.554373	22.741615
40.554367	22.7416067
40.554372	22.7416167

Using these values and with the help of Google My Maps, the scan area is accurately depicted on the map, as shown in the image below. The maximum depth was approximately 0.77 meters, while the minimum depth was 0.7 meters. The distances between the points were quite close, as can be clearly seen in the image, making the scanned area less easily distinguishable.
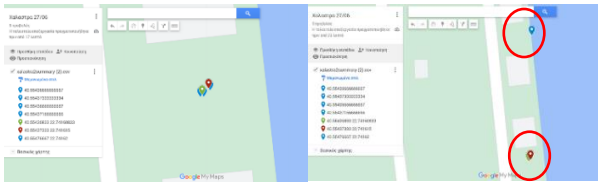

Fig. 13. Image of the map created on Google Maps from the measurements taken during the third excursion to Chalastra.

The image below shows a snapshot of all the scans conducted in the Chalastra area, providing an overview of the entire scan area.
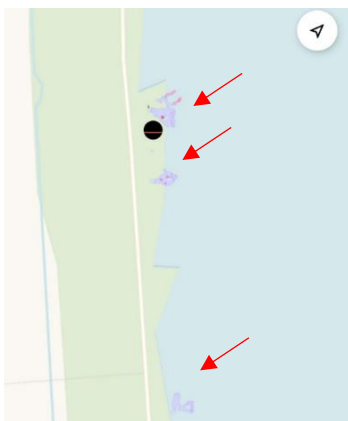

Fig. 14. Illustration of the complete scanning area of the Fishermen's Huts in Chalastra on a geographical map.

D. Fourth sounding scan at the port of Nea Michaniona

On July 11, 2024, the fourth excursion took place at the port of Nea Michaniona, Thessaloniki, to map a different area of the port than the one surveyed during the first excursion. The experimental procedure lasted about one hour and thirty minutes (09:30-11:00). This excursion was conducted in collaboration with students from abroad (Romania and Croatia), who participated in a Blended Intensive Programme under the Erasmus+ KA131 action. This time, the procedure was carried out differently. The students were divided into two groups, each scanning the area simultaneously, which resulted in measurements being collected from two different mobile devices. The following table shows indicative measurements from the scan file.

Table 9. Presentation of the measurements of the scan file at the port of Nea Michaniona.

Latitude	Longitude	Depth (m)	Temperature (ºC)
40.46146833	22.85848667	1.64	29
		1.67	29
		1.70	29
40.461465	22.85848167	1.71	29

The sea temperature ranged from 29°C to 30°C. The scan area, as determined by the sonar application, is presented below.
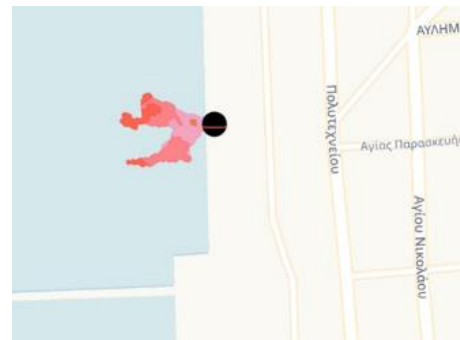

Fig. 15 Illustration of the scanning area of the port of Nea Michaniona on a geographical map.

The image below shows the final map of the port of Nea Michaniona, combining all the individual files.
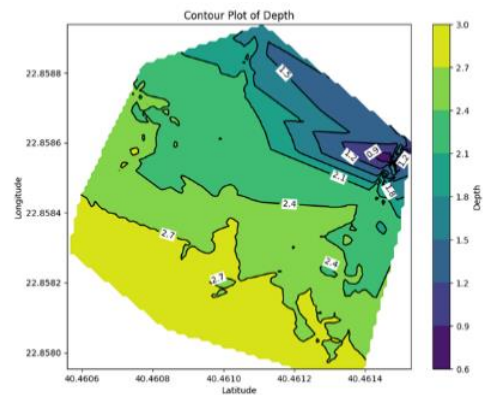

Fig. 16 Final bathymetric map of the port of Nea Michaniona during the fourth excursion.

By combining the .csv files from the two mobile phones and using the Laboratory's in-house Python code, the following table of points is generated.

Table 10. The four (4) corner points are derived from the .csv file generated by the program.

Latitude	Longitude
40.46055833	22.85829
40.46153	22.858605
40.4614	22.85795333
40.46110667	22.85894

Using these values and with the help of Google My Maps, the scan area is accurately depicted on the map, as shown in the image below. The total area scanned was 5.31 acres, with a maximum depth of 3 meters and a minimum depth of 0.9 meters.
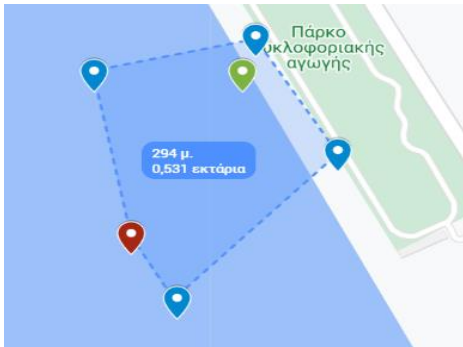

Fig. 17. Image of the final map as created in Google Maps from the measurements of the fourth excursion to Nea Michaniona.

The following image shows a snapshot of all the scans conducted in the area of Nea Michaniona, providing a relatively clear view of which parts of the port have been scanned.
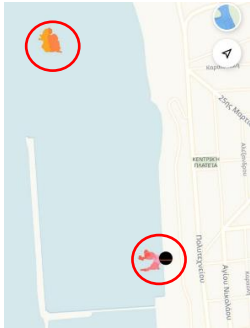

Fig. 18. Illustration of the entire scanning area of the port of Nea Michaniona on a geographical map.

E. Conclusions

The purpose of this article was to study, adjust, and experimentally operate a sonar system for scanning and mapping the seabed in real operational conditions. Specifically, during the study, bathymetric maps of two areas near the city of Thessaloniki were created using single-beam sonars and unmanned remotely controlled surface vehicles from the "Hippalus" Research Group of the International Hellenic University. Field measurements were conducted from April to July 2024. A total of four excursions were carried out: two at the port of Nea Michaniona and two at the Fishermen's Huts in Chalastra. In the port of Nea Michaniona, the maximum depth measured was 3.9 meters, and the minimum depth was 0.9 meters. In the bay of the Fishermen's Huts in Chalastra, the maximum depth measured was 1.9 meters, and the minimum depth was 0.8 meters. Important data on sea temperatures were also collected. The total area scanned in the port of Nea Michaniona was 9.17 acres. The application of the single-beam sonar proved to be a reliable tool for fast and efficient measurements at varying depths, although the accuracy of its data depends on sea conditions and the proper setup of the equipment.

IV. COPYRIGHT

REFERENCES

[1] F. A. Molland, "Underwater vehicles in The Maritime Engineering " in *Reference Book: A Guide to Ship Design, Construction and Operation*, ed: Springer, 2008.

[2] F. Remouit, "Underwater electrical connections and remotely operated vehicles," Licentiate (Diploma), Department of Engineering Sciences, Uppsala University, 2016.

[3] X. Li, J. Liu, L. Yan, S. Han, and X. Guan, "Relay Selection for Underwater Acoustic Sensor Networks: A Multi-User Multi-Armed Bandit Formulation," *SPECIAL SECTION ON UNDERWATER WIRELESS COMMUNICATIONS AND NETWORKING,* vol. IEEE Access 6, pp. 7839-7853, 2018.

[4] Deeper. (11.03.2024). *Deeper Sonar PRO+, Technical specifications.* Available: https://deepersonar.com/products/deeper-sonar-pro-2

[5] BlueRobotics. (29.09.2024). *A Smooth Operator's Guide to Underwater Sonars and Acoustic Devices.* Available: https://bluerobotics.com/learn/a-smooth-operators-guide-to-underwater-sonars-and-acoustic-devices/#echosounders

[6] R. Chinicz and R. Diamant, "A Statistical Evaluation of the Connection between Underwater Optical and Acoustic Images," *Remote Sensing,* vol. 16, 2024.

[7] A. L. Diaz, A. E. Ortega, H. Tingle, A. Pulido, and O. Cordero, "The Bathy-Drone: An Autonomous Uncrewed Drone-Tethered Sonar System," *Drones,* vol. 6, 2022.

[8] Chasing. (03.03.2024). *Chasing F1 Technical specifications.* Available: https://www.chasing.com/en/chasing-f1-pro-overview.html